UNIVERSIDAD DE CONCEPCIÓN

Centro de Investigación en Ingeniería Matemática (CI^{2}MA)

Mixed finite element methods for coupled fluid flow problems arising from reverse osmosis modeling

Isaac Bermudez, Víctor Burgos,
Jessika Camaño, Fernando Gajardo,
Ricardo Oyarzúa, Manuel Solano

PREPRINT 2024-15

SERIE DE PRE-PUBLICACIONES

Mixed finite element methods for coupled fluid flow problems arising from reverse osmosis modeling *

Isaac Bermúdez[1,2], Víctor Burgos[1,2], Jessika Camaño[3,2], Fernando Gajardo[4], Ricardo Oyarzúa[4,2], and Manuel Solano[1,2]

[1]Departamento de Ingeniería Matemática, Facultad de Ciencias Físicas y Matemáticas, Universidad de Concepción, Concepción, Chile. {ibermudez,msolano,vicburgos}@udec.cl

[2]Centro de Investigación en Ingeniería Matemática (CI^{2}MA), Universidad de Concepción, Concepción, Chile

[3]Grupo de Investigación en Análisis Numérico y Cálculo Científico (GIANuC^2), Departamento de Matemática y Física Aplicadas, Universidad Católica de la Santísima Concepción,Concepción, Chile, jecamano@ucsc.cl

[4]Grupo de Investigación en Métodos Numéricos y Aplicaciones (GIMNAP)-Departamento de Matemática, Universidad del Bío-Bío, Concepción, Chile, {royarzua,ferngajardo}@ubiobio.cl

June 25, 2024

Abstract

We consider a mathematical model for addressing coupled fluid flow problems arising from reverse osmosis modeling in water desalination processes. It consists of the coupled Navier Stokes/transport and Brinkman–Forchheimer/transport equations, with nonlinear conditions across a semi-permeate membrane. The cases of a single desalination channel and coupled feed/permeate channels are covered. To solve these partial differential equations, we employ a new mixed finite element method able to capture several variables of interest such as the salt concentration level, pressure drop and fluid velocity. Through diverse numerical simulations and a variety of configurations, we illustrate the capability of the method to accurately capture the behaviour of saline water when passing through membrane-based reverse osmosis desalination channels.

Key words: Brinkman–Forchheimer, Navier–Stokes, transport, mixed finite element methods, nonlinear transmission conditions, reverse osmosis, water desalination

1 Introduction

According to [14], the total volume of freshwater stocks is around the 2.5% (35 million km^3) of the total stock of water in the hydrosphere. Moreover, a large fraction of the freshwater (24 million km^3, or 68.7%) is in the form of ice and permanent snow cover in the Antarctic and Arctic regions. The rising apprehension regarding the future accessibility of freshwater resources has led to a surge in the establishment of seawater desalination plants. Furthermore, the development of membrane-based desalination methods has received special attention in recent years as a prominent solution to address the global challenge of water scarcity, due to their notable advantages, which include relatively low energy consumption compared to thermal-based techniques like multi-stage flash [27], as well as their capability to use renewable or low-grade energy sources [2, 29]. In this regard, reverse osmosis (RO) takes a prominent position, being employed in 69% of industrial desalination plants globally [11]. As the most energy-efficient desalination process, the membrane technology associated with RO is currently the subject of extensive research.

The main purpose of RO is removing all colloidal matter and dissolved particles larger than 0.1-1.0 nm in size from a liquid solution [27]. The conventional process includes three major stages. The initial phase, known as pre-treatment, focuses on the removal of coarse solids such as algae and smaller solid particles like fine sand

*Supported by ANID-Chile through Anillo of Computational Mathematics for Desalination Processes (ACT210087); FONDECYT projects 1231336 and 1240183; BASAL Project FB210005; and Beca Doctorado Nacional 21210582.

(see Figure 1 in [27]). Once seawater has undergone this pre-treatment, the main RO stage begins. At this point, pre-treated water flows at high pressure through the feed channel, allowing the water to pass through the pores of the semi-permeable membrane housed in a membrane module (see Figure 2 in [27]). Finally, the post-treatment stage is conducted to achieve mineral enrichment by introducing ions, such as magnesium and calcium, to the permeate water. This three-stage process ensures effective water purification through RO technology.

However, a major challenge in these separation processes is concentration polarization, which induces fouling (the undesired accumulation of materials) and reduces flux at the membrane. This phenomenon occurs because solutes are rejected at the membrane wall while convective transport delivers solutes to the membrane surface faster than diffusive transport can return them to the bulk streamflow. As a result, the solute concentration significantly increases at the membrane surface. To address this issue, spacers are introduced to keep the membrane layers separated and enhance mass transfer, thereby reducing concentration polarization at the wall [26]. Research on spacer filament distribution and design structure has notably increased over the past decade, aiming to identify optimal configurations based on specific requirements. Notable contributions in this field include works by [1, 8, 17, 18, 22, 28], among others. In this context, and to contribute to a better understanding of the processes underlying RO technology, we propose new numerical discretizations to accurately simulate three scenarios. The first scenario includes explicit spacers (small obstacles) located inside the desalination channels. The second scenario features a channel without spacers (from now on referred as empty channel). The third scenario emulates the effect of spacers implicitly by distributing their effect in the entire region and modeling the domain of simulation as a porous medium. For the first scenario, we employ the coupled Navier-Stokes/transport equations for simulation, while the Brinkman–Forchheimer/transport equations model is used for the third scenario.

Regarding the proposed numerical scheme, motivated by the Neumann type conditions at the outlet specified in (2.2), we adopt the well-established *mixed finite element method*. This approach involves rewriting the set of partial differential equations as a first-order system by introducing additional unknowns. The resulting equations are then discretized using well-known polynomial spaces, such as the Raviart-Thomas element space (see [12]). The mixed finite element method offers several advantages. It allows for the direct approximation of additional variables of interest, such as the salt concentration gradient and the gradient of the velocity of the fluid, without the need for numerical differentiation. Moreover, it enables the exact conservation of crucial properties such as momentum and mass (see [6, 7]).

Since we adopt a mixed finite element approach, due to technical reasons discussed in [3] (see also [13]), it is necessary to include a Lagrange multiplier to address the salt concentration constraint where the membrane is located. The non-linearity at the interface is then handled with this further unknown, and a suitable linearization is necessary to carry out the fixed-point iteration of the global problem. This paper gives a detailed explanation of the numerical models to be considered, as well as their discrete formulations and their respective matrix block structures. In addition, we performed several numerical simulations for different scenarios in order to show the applicability of the method. In particular, we will first consider simulations in a single channel, which are commonly reported in the literature. In addition, we will numerically study the case of two coupled feed and permeate channels, that to the best of our knowledge no benchmarks are available in the literature.

The manuscript is structured as follows. In Section 2 we introduce the model problem of interest in a single channel and define the unknowns to be considered in the variational formulation. Subsequently, in the same section we set the saddle point structure of the discrete variational system and its corresponding matrix block structure. Additionally, the mixed finite element discretization in two coupled domains is explained and its resolution strategy by means of a fixed point algorithm is carried out. Next, numerical simulations that illustrate the applicability of the methods and a detailed discussion are reported in Section 3. Finally, we conclude the study providing final remarks in Section 4.

We end this section by introducing some notations to be employed in the forthcoming sections. For any vector fields $\mathbf{v} = (v_1, v_2)^t$ and $\mathbf{w} = (w_1, w_2)^t$ we set the gradient and divergence operators, as

$$\nabla \mathbf{v} := \left(\frac{\partial v_i}{\partial x_j} \right)_{i,j=1,2}, \quad \text{and} \quad \mathrm{div}(\mathbf{v}) := \sum_{j=1}^{2} \frac{\partial v_j}{\partial x_j}.$$

In addition, for any tensor fields $\boldsymbol{\tau} = (\tau_{ij})_{i,j=1,2}$ and $\boldsymbol{\zeta} = (\zeta_{ij})_{i,j=1,2}$, we let $\mathbf{div}(\boldsymbol{\tau})$ be the divergence operator div acting along the rows of $\boldsymbol{\tau}$, and define the transpose, the trace, the tensor inner product, and the deviatoric

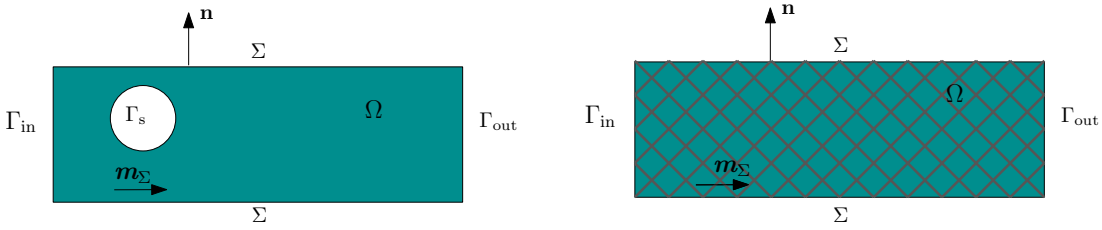

Figure 2.1: Sketch of a single channel with explicit spacer (left) and implicit spacers (right).

tensor, respectively, as

$$\boldsymbol{\tau}^t := (\boldsymbol{\tau}_{ji})_{i,j=1,2}, \quad \mathrm{tr}(\boldsymbol{\tau}) := \sum_{i=1}^{2} \tau_{ii}, \quad \boldsymbol{\tau} : \boldsymbol{\zeta} := \sum_{i,j=1}^{2} \tau_{ij}\zeta_{ij}, \quad \text{and } \boldsymbol{\tau}^{\mathrm{d}} := \boldsymbol{\tau} - \frac{1}{2}\mathrm{tr}(\boldsymbol{\tau})\mathbb{I}, \tag{1.1}$$

where $\mathbb{I}$ is the identity tensor in $\mathbb{R}^{2\times 2}$. Finally, given any generic scalar functional space M, we let $\mathbf{M}$ and $\mathbb{M}$ be the corresponding vector and tensor-valued counterparts.

2 Theoretical description

2.1 A single channel

Brinkman–Forchheimer/transport equations. Let Ω be a bounded polygonal domain in $\mathbb{R}^2$ with boundary $\partial\Omega$ as shown in Figure 2.1 and assume that the boundary is decomposed into an inlet Γ_{in}, an outlet Γ_{out}, and two portions describing the membrane, denoted by Σ, i.e., $\partial\Omega = \overline{\Gamma}_{\mathrm{in}} \cup \overline{\Gamma}_{\mathrm{out}} \cup \overline{\Sigma}$. In addition, we denote by $\mathbf{n}$ the unit outward normal vector on $\partial\Omega$ and by $\boldsymbol{m}_\Sigma$ the tangent vector on Σ. The mathematical model describing the behavior of saline water in a RO module consists of a coupled set of partial differential equations where the Brinkman–Forchheimer equations, used to describe the fluid dynamics, are coupled with a transport equation employed to model the concentration of salt within the channel Ω. More precisely, we consider the following coupled system of equations

$$\begin{aligned} -\nu\,\triangle\frac{\widehat{\mathbf{u}}}{\varepsilon} + \rho\,\mathbf{div}\Big(\frac{\widehat{\mathbf{u}}}{\varepsilon}\otimes\frac{\widehat{\mathbf{u}}}{\varepsilon}\Big) + \nabla p = -\widehat{\mathtt{D}}\widehat{\mathbf{u}} - \widehat{\mathtt{F}}|\widehat{\mathbf{u}}|\widehat{\mathbf{u}}, \quad \mathrm{div}\Big(\frac{\widehat{\mathbf{u}}}{\varepsilon}\Big) = 0 \quad \text{in} \quad \Omega, \\ -\kappa\,\triangle\phi + \frac{\widehat{\mathbf{u}}}{\varepsilon}\cdot\nabla\phi = 0 \quad \text{in} \quad \Omega, \end{aligned} \tag{2.1}$$

where $\widehat{\mathbf{u}}$ is the fluid velocity, p the fluid pressure and ϕ the salt concentration occupying the domain Ω. The given data are the fluid dynamic viscosity ν, the fluid density ρ, the solute diffusivity through the solvent κ and the porosity of the medium ε. All these parameters are assumed to be positive constants. In turn, $\widehat{\mathtt{D}}$ and $\widehat{\mathtt{F}}$ are the Darcy and Forchheimer coefficients, respectively, assumed to be either positive constants or equal to zero. The case where $\widehat{\mathtt{D}} > 0$ and $\widehat{\mathtt{F}} > 0$ will be used to describe the situation with implicit spacers. Conversely, when $\widehat{\mathtt{D}}$ and $\widehat{\mathtt{F}}$ are zero, the system (2.1) reduces to the Navier–Stokes/transport problem, which will be used to describe the case with explicit spacers. For the sake of simplicity, in what follows, we introduce the changes of variables $\mathbf{u} := \widehat{\mathbf{u}}/\epsilon$, $\mathtt{D} := \varepsilon\,\widehat{\mathtt{D}}$ and $\mathtt{F} := \varepsilon^2\,\widehat{\mathtt{F}}$.

We complement these equations with suitable boundary conditions on each part of the boundary as described as follows.

Inlet and outlet boundaries. In the inlet boundary Γ_{in}, we consider a given velocity profile $\mathbf{u}_{\mathrm{in}}$ and constant concentration ϕ_{in}. In the outlet of the channel, denoted by Γ_{out}, we consider a do-nothing boundary condition and zero diffusion of salt. That is

$$\mathbf{u} = \mathbf{u}_{\mathrm{in}}, \quad \phi = \phi_{\mathrm{in}} \quad \text{on} \quad \Gamma_{\mathrm{in}} \quad \text{and} \quad (\nu\nabla\mathbf{u} - p\mathbb{I})\mathbf{n} = \mathbf{0}, \quad \kappa\nabla\phi\cdot\mathbf{n} = 0 \quad \text{on} \quad \Gamma_{\mathrm{out}}. \tag{2.2}$$

Remark 1. As noticed in [21, Section 1] (see also [22, Section 2.2]), the open boundary condition (second equation in (2.2)), is usually considered thinking of truncating a bigger physical domain (e.g., outflow profile for flow in a bifurcated channel), allowing the fluid to flow naturally.

Imperfect membrane boundary conditions. At membrane surface, velocity and salt concentration are coupled through the following relations (see [8])

$$\mathbf{u}\cdot\boldsymbol{m}_{\Sigma}=0,\quad \mathbf{u}\cdot\mathbf{n}=c_0-c_1\,\phi\,,\quad (\phi\mathbf{u}-\kappa\nabla\phi)\cdot\mathbf{n}\;=\;c_2\phi\quad\text{on}\quad\Sigma,$$

where $c_0 := A\Delta P$, $c_1 := AiRT$ and $c_2 := B$ are positive constants specified later on in Table 3.1. Notice that, a simple algebraic manipulation allows us to rewrite this condition as follows:

$$\mathbf{u}\cdot\boldsymbol{m}_{\Sigma}=0,\quad \mathbf{u}\cdot\mathbf{n}=c_0-c_1\phi\,,\quad \kappa\nabla\phi\cdot\mathbf{n}+c_1\phi^2+c_3\phi\;=\;0\quad\text{on}\quad\Sigma,\tag{2.3}$$

where $c_3 = c_2 - c_0$.

We conclude this section by outlining the considerations to be taken into account when using either explicit or implicit spacers.

Explicit spacers. Explicit spacers are obstacles placed inside the channel with the aim of enhancing the permeate flux. These obstacles are assumed to have a circular shape with boundary Γ_{s} (see Figure 2.1).

As previously mentioned, when introducing explicit spacers in the channel, $\widehat{\mathtt{D}}$ and $\widehat{\mathtt{F}}$ are set to zero, reducing the set of equations (2.1) to a Navier–Stokes/transport coupled problem. Additionally, on Γ_{s}, the following boundary conditions must be considered (see [8]):

$$\kappa\nabla\phi\cdot\mathbf{n}=0\quad\text{on}\quad\Gamma_{\mathrm{s}}\quad\text{and}\quad\mathbf{u}=\mathbf{0}\quad\text{on}\quad\Gamma_{\mathrm{s}}.\tag{2.4}$$

Implicit spacers. In the second scenario, the spacers are treated implicitly. In this case, we consider $\Gamma_{\mathrm{s}} = \emptyset$ and the effect of the spacers is emulated by making the fluid to flow through a porous media. This means we solve the Darcy–Forchheimer equation, where $\widehat{\mathtt{D}} := \dfrac{\nu}{\widehat{K}}$ and $\widehat{\mathtt{F}} := \dfrac{1.75\,\rho\,\varepsilon}{\sqrt{150\,\varepsilon^3\widehat{K}}}$ are the Darcy and Forchheimer coefficients [23, 24], and $\widehat{K}$ and ε, are the porous medium permeability and the porosity of the medium, respectively. In turn, we keep in mind that spacers are treated implicitly. That is, if we want to emulate the effect of $\mathtt{N_{sp}}$ spacers of diameter d_{s}, the porosity of the medium can be calculated as [19, eq. (1)]

$$\varepsilon=\frac{\mathtt{A_{tot}}-\mathtt{A_{sp}}}{\mathtt{A_{tot}}}=\frac{\mathtt{A_{tot}}-\mathtt{N_{sp}}\pi(0.25)d_{\mathrm{s}}^2}{\mathtt{A_{tot}}},\tag{2.5}$$

where $\mathtt{A_{tot}}$ and $\mathtt{A_{sp}}$ stand for the total area of the domain and the area occupied for the spacers, respectively. Next, the permeability is determined using the Kozeny–Carman equation [25, Section 2]

$$\widehat{K}\;=\;\Phi^2\frac{d_{\mathrm{s}}^2}{180}\frac{\varepsilon^3}{(1-\varepsilon)^2},\tag{2.6}$$

where Φ is the sphericity of the particle forming the porous media.

Remark 2. Numerical simulations considering a model of implicit spacers require less computational effort compared to the case of explicit spacers, because the latter configuration need a finer mesh near the spacers. However, the price to pay is that the implicit spacers model cannot detect the local effect of the spacers, since their influence is being averaged along the channel. In fact, the porous medium emulating the effect of the spacers, only takes into account the number of spacers but not their distribution in the channel. We will go back to this point in the numerical simulation section.

2.1.1 Mixed finite element discretization.

We propose a mixed finite element discretization to approximate the solution of the coupled system (2.1)–(2.3). To that end, and as previously mentioned in Section 1, we introduce further unknowns and rewrite the system of equations as a first-order set of equations. In fact, we let $\boldsymbol{\sigma} := \nu\nabla\mathbf{u} - p\mathbb{I}$ and $\mathbf{t} := \kappa\nabla\phi$ and proceed similarly to [9] to rewrite (2.1) equivalently as follows

$$\frac{1}{\nu}\boldsymbol{\sigma}^{\mathtt{d}}=\nabla\mathbf{u},\quad \mathbf{div}(\boldsymbol{\sigma})-\frac{\rho}{\nu}\boldsymbol{\sigma}^{\mathtt{d}}\,\mathbf{u}\,-\mathtt{D}\mathbf{u}-\mathtt{F}|\mathbf{u}|\mathbf{u}\;=\;\mathbf{0},\quad \mathbf{t}=\kappa\,\nabla\phi\quad\text{and}\quad\kappa\,\mathrm{div}(\mathbf{t})=\mathbf{u}\cdot\mathbf{t}.\tag{2.7}$$

We observe that employing the incompressibility condition $\mathrm{div}(\mathbf{u}) = 0$ in Ω, we have eliminated the pressure from the system (see [13] for more details), which however can be recovered by means of the postprocessing formula

$$p = -\frac{1}{2}\mathrm{tr}(\boldsymbol{\sigma}).$$

In turn, using these new variables $\boldsymbol{\sigma}$ and $\mathbf{t}$, we rewrite (2.2) as

$$\mathbf{u} = \mathbf{u}_{\mathrm{in}} \quad \text{on} \quad \Gamma_{\mathrm{in}}, \quad \boldsymbol{\sigma}\mathbf{n} = \mathbf{0} \quad \text{on} \quad \Gamma_{\mathrm{out}}, \quad \phi = \phi_{\mathrm{in}} \quad \text{on} \quad \Gamma_{\mathrm{in}} \quad \text{and} \quad \mathbf{t}\cdot\mathbf{n} = 0 \quad \text{on} \quad \Gamma_{\mathrm{out}}. \tag{2.8}$$

Finally, due to technical reasons discussed in [3] and [13], we let $\Gamma^{\mathrm{c}}_{\mathrm{in}} := \partial\Omega\backslash\Gamma_{\mathrm{in}}$ and introduce the additional variable $\xi := -\phi|_{\Gamma^{\mathrm{c}}_{\mathrm{in}}}$, known as Lagrange multiplier in the context of mixed finite element methods. Then, rewrite (2.3) as

$$\mathbf{u}\cdot\boldsymbol{m}_{\Sigma} = 0, \quad \mathbf{u}\cdot\mathbf{n} = c_0 + c_1\xi\,, \quad \mathbf{t}\cdot\mathbf{n} + c_1\xi^2 - c_3\xi = 0 \quad \text{on} \quad \Sigma. \tag{2.9}$$

Now, we let $\{\mathcal{T}_h\}_{h>0}$ be a family of shape regular partition of the domain Ω formed by triangles K of diameter h_K, and denote by $h := \max\{h_K : K \in \mathcal{T}_h\}$ its corresponding meshsize. On each K we define the local Raviart-Thomas element of order 0 as (see [12] for further details)

$$\mathbf{RT}_0(K) := \left\{\mathbf{v} : K \to \mathbb{R}^2 : \mathbf{v}(x_1,x_2) := \begin{pmatrix} a \\ b \end{pmatrix} + c\begin{pmatrix} x_1 \\ x_2 \end{pmatrix}, \quad a,b,c \in \mathbb{R}\right\},$$

and denote by $\mathrm{P}_0(K)$ the spaces of polynomials of degree 0 in K. Then, we introduce, respectively, the following finite element spaces for the variables $\mathbf{t}$, $\boldsymbol{\sigma}$, ϕ and $\mathbf{u}$:

$$\begin{aligned}
\mathbf{H}_h &:= \left\{\mathbf{s} : \Omega \to \mathbb{R}^2 : \ \mathbf{s}|_K \in \mathbf{RT}_0(K) \quad \forall\, K \in \mathcal{T}_h\right\}, \\
\mathbb{H}_h &:= \left\{\boldsymbol{\tau} = (\boldsymbol{\tau}_{ij}) : \Omega \to \mathbb{R}^{2\times 2} : \ (\boldsymbol{\tau}_{i,1}, \boldsymbol{\tau}_{i,2})^t \in \mathbf{H}_h,\, i \in \{1,2\} \quad \text{and} \quad \boldsymbol{\tau}\mathbf{n} = \mathbf{0} \quad \text{on} \quad \Gamma_{\mathrm{out}}\right\}, \\
\mathrm{X}_h &:= \{\psi : \Omega \to \mathbb{R} : \ \psi|_K \in \mathrm{P}_0(K) \quad \forall\, K \in \mathcal{T}_h\}, \\
\mathbf{Q}_h &:= \{\mathbf{v} = (v_1,v_2)^t : \Omega \to \mathbb{R}^2 : \ v_i \in \mathrm{X}_h,\, i \in \{1,2\}\}.
\end{aligned} \tag{2.10}$$

It remains to introduce the finite element space to approximate the Lagrange multiplier ξ. To that end, we proceed similarly to [13] and denote by $\Gamma^{\mathrm{c}}_{\mathrm{in},h}$ the partition of $\Gamma^{\mathrm{c}}_{\mathrm{in}}$ inherited from $\mathcal{T}_h$. Let us assume, without loss of generality, that the number of edges of $\Gamma^{\mathrm{c}}_{\mathrm{in},h}$ is even. Then, we let $\Gamma^{\mathrm{c}}_{\mathrm{in},2h}$ be the partition of $\Gamma^{\mathrm{c}}_{\mathrm{in}}$ arising by joining pairs of adjacent edges of $\Gamma^{\mathrm{c}}_{\mathrm{in},h}$. If the number of edges of $\Gamma^{\mathrm{c}}_{\mathrm{in},h}$ is odd, we simply reduce it to the even case by adding one node to the discretization of the interface and locally modify the triangulation to keep the mesh conformity and regularity. According to the above, we define the following finite element space for the unknown ξ:

$$\mathrm{M}_h := \left\{\eta_h \in \mathcal{C}(\Gamma^{\mathrm{c}}_{\mathrm{in}}) : \quad \eta_h|_e \in \mathrm{P}_1(e) \quad \forall \text{ edge } e \in \Gamma^{\mathrm{c}}_{\mathrm{in},2h}\right\},$$

where $\mathrm{P}_1(e)$ is the space of linear polynomials defined on an edge e of $\Gamma^{\mathrm{c}}_{\mathrm{in},2h}$. In this way, having introduced the finite element spaces for each unknown, the discrete nonlinear system of equations to approximate the solution of (2.7)–(2.9), reads: Find $\boldsymbol{\sigma}_h \in \mathbb{H}_h$, $\mathbf{u}_h \in \mathbf{Q}_h$, $\mathbf{t}_h \in \mathbf{H}_h$, $\phi_h \in \mathrm{X}_h$ and $\xi_h \in \mathrm{M}_h$, such that

$$\frac{1}{\nu}\int_\Omega \boldsymbol{\sigma}^{\mathtt{d}}_h : \boldsymbol{\tau}_h + \int_\Omega \mathbf{u}_h\cdot\mathbf{div}\boldsymbol{\tau}_h = \int_{\Gamma^{\mathrm{c}}_{\mathrm{out}}} (\boldsymbol{\tau}_h\mathbf{n})\cdot\mathbf{u}_{\mathrm{D},\,\xi_h} \quad \forall \boldsymbol{\tau}_h \in \mathbb{H}_h, \tag{2.11}$$

$$\int_\Omega \mathbf{v}_h\cdot\mathbf{div}\boldsymbol{\sigma}_h - \mathtt{D}\int_\Omega \mathbf{u}_h\cdot\mathbf{v}_h - \mathtt{F}\int_\Omega |\mathbf{u}_h|\mathbf{u}_h\cdot\mathbf{v}_h - \frac{\rho}{\nu}\int_\Omega \boldsymbol{\sigma}^{\mathtt{d}}_h\mathbf{u}_h\cdot\mathbf{v}_h = 0 \quad \forall \mathbf{v}_h \in \mathbf{Q}_h, \tag{2.12}$$

$$\frac{1}{\kappa}\int_\Omega \mathbf{t}_h\cdot\mathbf{s}_h + \int_\Omega \phi_h\mathrm{div}\mathbf{s}_h + \int_{\Gamma^{\mathrm{c}}_{\mathrm{in}}} (\mathbf{s}_h\cdot\mathbf{n})\xi_h = 0 \quad \forall \mathbf{s}_h \in \mathbf{H}_h, \tag{2.13}$$

$$\int_\Omega \psi_h\mathrm{div}\mathbf{t}_h - \frac{1}{\kappa}\int_\Omega \mathbf{u}_h\cdot\mathbf{t}_h\psi_h = 0 \quad \forall \psi_h \in \mathrm{X}_h, \tag{2.14}$$

$$\int_{\Gamma^{\mathrm{c}}_{\mathrm{in}}} (\mathbf{t}_h\cdot\mathbf{n})\eta_h - c_3\int_\Sigma \xi_h\eta_h + c_1\int_\Sigma \xi_h^2\,\eta_h = 0 \quad \forall \eta_h \in \mathrm{M}_h, \tag{2.15}$$

where for each $\chi_h \in \mathrm{M}_h$, $\mathbf{u}_{\mathrm{D},\chi_h}$ is defined as:

$$\mathbf{u}_{\mathrm{D},\chi_h} = \begin{cases} \mathbf{u}_{\mathrm{in}} & \text{on} \quad \Gamma_{\mathrm{in}}, \\ (c_1\chi_h + c_0)\mathbf{n} & \text{on} \quad \Sigma. \end{cases} \tag{2.16}$$

We observe that equations (2.11), (2.12), (2.13) and (2.14) correspond to the discretization of the first, second, third and fourth equations of (2.7), respectively, whereas (2.15) is the discrete version of the third equation of (2.9).

Remark 3. When introducing explicit spacers in the channel, the boundary conditions set in (2.4), which are rewritten as

$$\mathbf{t}\cdot\mathbf{n} = 0 \quad \text{on} \quad \Gamma_{\mathrm{s}} \quad \text{and} \quad \mathbf{u} = \mathbf{0} \quad \text{on} \quad \Gamma_{\mathrm{s}}, \tag{2.17}$$

suggest to slightly modify the third term of (2.13), the first term of (2.15) and the boundary datum $\mathbf{u}_{\mathrm{D},\chi_h}$ by

$$\int_{\Gamma_{\mathrm{in}}^{\mathrm{c}}\cup\Gamma_{\mathrm{s}}} (\mathbf{s}_h\cdot\mathbf{n})\xi_h, \quad \int_{\Gamma_{\mathrm{in}}^{\mathrm{c}}\cup\Gamma_{\mathrm{s}}} (\mathbf{t}_h\cdot\mathbf{n})\eta_h \quad \text{and} \quad \mathbf{u}_{\mathrm{D},\chi_h} = \begin{cases} \mathbf{0} & \text{on} \quad \Gamma_{\mathrm{s}}, \\ \mathbf{u}_{\mathrm{in}} & \text{on} \quad \Gamma_{\mathrm{in}}, \\ (c_1\chi_h + c_0)\mathbf{n} & \text{on} \quad \Sigma, \end{cases}$$

respectively.

2.1.2 Solving strategy.

The nonlinear numerical scheme (2.11)–(2.15) will be solved by a fixed point iteration. To explain clearly this strategy, and for the sake of presentation, we will express the set of equations in a block structure. We begin by noticing that the discrete system can be rewritten more compactly as follows: Find $\boldsymbol{\sigma}_h \in \mathbb{H}_h$, $\mathbf{u}_h \in \mathbf{Q}_h$, $\mathbf{t}_h \in \mathbf{H}_h$, $\phi_h \in \mathrm{X}_h$, $\xi_h \in \mathrm{M}_h$, such that

$$\begin{array}{llll} \mathbf{a}_{\mathbf{S}}(\boldsymbol{\sigma}_h,\boldsymbol{\tau}_h) + \mathbf{b}_{\mathbf{S}}(\boldsymbol{\tau}_h,\mathbf{u}_h) & & = \mathbf{F}(\xi_h;\boldsymbol{\tau}_h) & \forall\, \boldsymbol{\tau}_h \in \mathbb{H}_h, \\ \mathbf{b}_{\mathbf{S}}(\boldsymbol{\sigma}_h,\mathbf{v}_h) - \mathbf{d}_{\mathbf{S}}(\mathbf{u}_h;\mathbf{u}_h,\mathbf{v}_h) & -\mathbf{O}_{\mathbf{S}}(\mathbf{u}_h;\boldsymbol{\sigma}_h,\mathbf{v}_h) & = 0 & \forall\, \mathbf{v}_h \in \mathbf{Q}_h, \\ \mathbf{a}_{\mathbf{T}}(\mathbf{t}_h,\mathbf{s}_h) + \mathbf{b}_{\mathbf{T},1}(\mathbf{s}_h,\phi_h) & +\mathbf{b}_{\mathbf{T},2}(\mathbf{s}_h,\xi_h) & = 0 & \forall\, \mathbf{s}_h \in \mathbf{H}_h, \\ \mathbf{b}_{\mathbf{T},1}(\mathbf{t}_h,\psi_h) & -\mathbf{O}_{\mathbf{T}}(\mathbf{u}_h;\mathbf{t}_h,\psi_h) & = 0 & \forall\, \psi_h \in \mathrm{X}_h, \\ \mathbf{b}_{\mathbf{T},2}(\mathbf{t}_h,\eta_h) & -\mathbf{d}_{\mathbf{T}}(\xi_h,\eta_h) + \mathbf{C}_{\mathbf{T}}(\xi_h;\xi_h,\eta_h) & = 0 & \forall\, \eta_h \in \mathrm{M}_h. \end{array} \tag{2.18}$$

where $\mathbf{a}_{\mathbf{S}}(\cdot,\cdot)$, $\mathbf{b}_{\mathbf{S}}(\cdot,\cdot)$, $\mathbf{a}_{\mathbf{T}}(\cdot,\cdot)$, $\mathbf{b}_{\mathbf{T},1}(\cdot,\cdot)$, $\mathbf{b}_{\mathbf{T},2}(\cdot,\cdot)$ and $\mathbf{d}_{\mathbf{T}}(\cdot,\cdot)$ are the bilinear forms defined as

$$\begin{aligned} &\mathbf{a}_{\mathbf{S}}(\boldsymbol{\sigma}_h,\boldsymbol{\tau}_h) := \frac{1}{\nu}\int_\Omega \boldsymbol{\sigma}_h^{\mathtt{d}} : \boldsymbol{\tau}_h^{\mathtt{d}}, \quad \mathbf{b}_{\mathbf{S}}(\boldsymbol{\tau}_h,\mathbf{v}_h) := \int_\Omega \mathbf{u}_h\cdot\mathbf{div}(\boldsymbol{\tau}_h), \quad \mathbf{a}_{\mathbf{T}}(\mathbf{t}_h,\mathbf{s}_h) := \frac{1}{\kappa}\int_\Omega \mathbf{t}_h\cdot\mathbf{s}_h, \\ &\mathbf{b}_{\mathbf{T},1}(\mathbf{s}_h,\psi_h) := \int_\Omega \psi_h \mathrm{div}(\mathbf{s}_h), \quad \mathbf{b}_{\mathbf{T},2}(\mathbf{s}_h,\eta_h) := \int_{\Gamma_{\mathrm{in}}^{\mathrm{c}}} (\mathbf{s}_h\cdot\mathbf{n})\,\eta_h, \quad \mathbf{d}_{\mathbf{T}}(\xi_h,\eta_h) := c_3\int_\Sigma \xi_h\eta_h; \end{aligned} \tag{2.19}$$

and, for each $\chi_h \in \mathrm{M}_h$, $\mathbf{F}(\chi_h;\cdot)$ and $\mathbf{C}_{\mathbf{T}}(\chi_h;\cdot,\cdot)$ are given by

$$\mathbf{F}(\chi_h;\boldsymbol{\tau}_h) := \int_{\Gamma_{\mathrm{out}}^{\mathrm{c}}} (\boldsymbol{\tau}_h\mathbf{n})\,\mathbf{u}_{\mathrm{D},\chi_h}, \quad \mathbf{C}_{\mathbf{T}}(\chi_h;\xi_h,\eta_h) := c_1\int_\Sigma \chi_h\,\xi_h\,\eta_h. \tag{2.20}$$

For each $\mathbf{w}_h \in \mathbf{Q}_h$, $\mathbf{O}_{\mathbf{S}}(\mathbf{w}_h;\cdot,\cdot)$, $\mathbf{O}_{\mathbf{T}}(\mathbf{w}_h;\cdot,\cdot)$ and $\mathbf{d}_{\mathbf{S}}(\mathbf{w}_h;\cdot,\cdot)$ are defined by

$$\begin{aligned} &\mathbf{O}_{\mathbf{S}}(\mathbf{w}_h;\boldsymbol{\sigma}_h,\mathbf{v}_h) := \frac{\rho}{\nu}\int_\Omega \boldsymbol{\sigma}_h^{\mathtt{d}}\mathbf{w}_h\cdot\mathbf{v}_h, \quad \mathbf{O}_{\mathbf{T}}(\mathbf{w}_h;\mathbf{t}_h,\psi_h) := \frac{1}{\kappa}\int_\Omega \mathbf{w}_h\cdot\mathbf{t}_h\psi_h, \\ &\mathbf{d}_{\mathbf{S}}(\mathbf{w}_h;\mathbf{u}_h,\mathbf{v}_h) := \mathtt{D}\int_\Omega \mathbf{u}_h\cdot\mathbf{v}_h + \mathtt{F}\int_\Omega |\mathbf{w}_h|\mathbf{u}_h\cdot\mathbf{v}_h. \end{aligned} \tag{2.21}$$

In what follows, in abuse of notation, we denote by $\boldsymbol{\sigma}_h$, $\mathbf{u}_h$, $\mathbf{t}_h$, ϕ_h, and ξ_h the degrees of freedom associated to the unknowns of (2.18). In turn, $\mathbf{a}_{\mathbf{S}}$, $\mathbf{a}_{\mathbf{T}}$, $\mathbf{b}_{\mathbf{S}}$, $\mathbf{b}_{\mathbf{T},1}$, $\mathbf{b}_{\mathbf{T},2}$, $\mathbf{d}_{\mathbf{T}}$, $\mathbf{O}_{\mathbf{S}}(\mathbf{w}_h)$, $\mathbf{O}_{\mathbf{T}}(\mathbf{w}_h)$, $\mathbf{d}_{\mathbf{S}}(\mathbf{w}_h)$ and $\mathbf{C}_{\mathbf{T}}(\chi_h)$ will

denote the corresponding finite element matrices associated to the bilinear forms in (2.19)-(2.21), and $\mathbf{F}(\chi_h)$ will denote the vector associated to $\mathbf{F}(\chi_h;\cdot)$ defined in (2.20). Then from (2.18) we obtain the following system

$$\left(\begin{array}{c|c} \mathcal{A}_{\mathbf{S}}(\mathbf{u}_h) & \mathbf{0} \\ \hline \mathbf{0} & \mathcal{A}_{\mathbf{T}}(\mathbf{u}_h,\xi_h) \end{array}\right)\begin{pmatrix} \boldsymbol{\sigma}_h \\ \mathbf{u}_h \\ \mathbf{t}_h \\ \phi_h \\ \xi_h \end{pmatrix} = \begin{pmatrix} \mathbf{F}(\xi_h) \\ \mathbf{0} \\ \mathbf{0} \\ \mathbf{0} \end{pmatrix}, \tag{2.22}$$

where

$$\mathcal{A}_{\mathbf{S}}(\mathbf{u}_h) := \left(\begin{array}{c|c} \mathbf{a}_{\mathbf{S}} & \mathbf{b}_{\mathbf{S}} \\ \hline (\mathbf{b}_{\mathbf{S}})^t - \mathbf{O}_{\mathbf{S}}(\mathbf{u}_h) & -\mathbf{d}_{\mathbf{S}}(\mathbf{u}_h) \end{array}\right) \tag{2.23}$$

and

$$\mathcal{A}_{\mathbf{T}}(\mathbf{u}_h,\xi_h) := \left(\begin{array}{c|c|c} \mathbf{a}_{\mathbf{T}} & \mathbf{b}_{\mathbf{T},1} & \mathbf{b}_{\mathbf{T},2} \\ \hline (\mathbf{b}_{\mathbf{T},1})^t - \mathbf{O}_{\mathbf{T}}(\mathbf{u}_h) & \mathbf{0} & \mathbf{0} \\ \hline (\mathbf{b}_{\mathbf{T},2})^t & \mathbf{0} & -\mathbf{d}_{\mathbf{T}} + \mathbf{C}_{\mathbf{T}}(\xi_h) \end{array}\right). \tag{2.24}$$

Now we turn to explain the iterative scheme to solve (2.22). To that end, we let ξ_h^0 and $\mathbf{u}_h^0$ be initial guesses. Then, for each $n \geqslant 1$, first we solve the linear system: Find $(\boldsymbol{\sigma}_h^n, \mathbf{u}_h^n)$, such that

$$\mathcal{A}_{\mathbf{S}}(\mathbf{u}_h^{n-1})\begin{pmatrix} \boldsymbol{\sigma}_h^n \\ \mathbf{u}_h^n \end{pmatrix} = \begin{pmatrix} \mathbf{F}(\xi_h^{n-1}) \\ \mathbf{0} \end{pmatrix},$$

and after computing $\boldsymbol{\sigma}_h^n$ and $\mathbf{u}_h^n$, we solve the linear system: Find $(\mathbf{t}_h^n, \phi_h^n, \xi_h^n)$, such that

$$\mathcal{A}_{\mathbf{T}}(\mathbf{u}_h^n, \xi_h^{n-1})\begin{pmatrix} \mathbf{t}_h^n \\ \phi_h^n \\ \xi_h^n \end{pmatrix} = \begin{pmatrix} \mathbf{0} \\ \mathbf{0} \end{pmatrix}.$$

The iterative algorithm stops when certain criteria (see Section 3) is satisfied.

2.2 Coupled feed and permeate channels

We consider a model for two coupled channels where water with salt concentration flows through the feed channel Ω_{f} and passes through a membrane Σ to the permeate channel Ω_{p}. In order to describe the geometry, we let Ω_{f} and Ω_{p} be two bounded polygonal domains in R^2 such that $\partial\Omega_{\mathrm{f}} \cap \partial\Omega_{\mathrm{p}} = \Sigma \neq \emptyset$ and $\Omega_{\mathrm{f}} \cap \Omega_{\mathrm{p}} = \emptyset$, and set $\Omega := \Omega_{\mathrm{f}} \cup \Sigma \cup \Omega_{\mathrm{p}}$. In turn, for each $\star \in \{\mathrm{f},\mathrm{p}\}$ we denote $\Gamma_\star := \partial\Omega_\star \backslash \overline{\Sigma} = \Gamma_{\mathrm{in},\star} \cup \overline{\Gamma}_{\mathrm{w},\star} \cup \Gamma_{\mathrm{out},\star}$, where $\Gamma_{\mathrm{w},\star}$ denotes the top ($\star = \mathrm{f}$) and bottom ($\star = \mathrm{p}$) boundaries of the channel (see Figure 2.2), and by $\mathbf{n}_\star$ we denote the unit normal vector, which is chosen pointing outwards from $\Omega_\star$, thus $\mathbf{n}_{\mathrm{f}} = -\mathbf{n}_{\mathrm{p}}$ on Σ. We also consider a unit tangent vector $\boldsymbol{m}_\Sigma$ on Σ as in Figure 2.2. On each channel $\Omega_\star$, with $\star \in \{\mathrm{f},\mathrm{p}\}$, the fluid and salt concentration satisfy the equations stated in Section 2.1, and the boundary conditions at the inlet and outlet are the ones specified in equations (2.2). More precisely, after introducing the further variables $\boldsymbol{\sigma}_\star := \nu_\star \nabla \mathbf{u}_\star - p_\star \mathbb{I}$ and $\mathbf{t}_\star := \kappa_\star \nabla \phi_\star$ in $\Omega_\star$ ($\star \in \{\mathrm{f},\mathrm{p}\}$), we consider the first-order set of equations:

$$\begin{gathered} \frac{1}{\nu}\boldsymbol{\sigma}_\star^{\mathtt{d}} = \nabla \mathbf{u}_\star, \quad \mathbf{div}(\boldsymbol{\sigma}_\star) - \frac{\rho}{\nu}\boldsymbol{\sigma}_\star^{\mathtt{d}}\,\mathbf{u}_\star - \mathtt{D}\mathbf{u}_\star - \mathtt{F}|\mathbf{u}_\star|\mathbf{u}_\star = \mathbf{0}, \\ \mathbf{t}_\star = \kappa\,\nabla\phi_\star \quad \text{and} \quad \kappa\,\mathrm{div}(\mathbf{t}_\star) = \mathbf{u}_\star \cdot \mathbf{t}_\star, \end{gathered} \tag{2.25}$$

and on $\Gamma_{\mathrm{in},\star}$ and $\Gamma_{\mathrm{out},\star}$, we consider the boundary conditions

$$\begin{gathered} \mathbf{u}_\star = \mathbf{u}_{\mathrm{in},\star} \quad \text{on} \quad \Gamma_{\mathrm{in},\star}, \quad \boldsymbol{\sigma}_\star \mathbf{n}_\star = \mathbf{0} \quad \text{on} \quad \Gamma_{\mathrm{out}_\star}, \\ \phi_\star = \phi_{\mathrm{in},\star} \quad \text{on} \quad \Gamma_{\mathrm{in},\star} \quad \text{and} \quad \mathbf{t}_\star \cdot \mathbf{n}_\star = 0 \quad \text{on} \quad \Gamma_{\mathrm{out},\star}. \end{gathered} \tag{2.26}$$

Both channels are coupled through a membrane Σ by means of the transmission conditions :

$$\begin{gathered} \mathbf{u}_\star \cdot \boldsymbol{m}_\Sigma = 0, \quad \mathbf{u}_{\mathrm{f}} \cdot \mathbf{n}_{\mathrm{f}} = -\mathbf{u}_{\mathrm{p}} \cdot \mathbf{n}_{\mathrm{p}}, \quad \mathbf{u}_{\mathrm{f}} \cdot \mathbf{n}_{\mathrm{f}} = c_0 - c_1(\phi_{\mathrm{f}} - \phi_{\mathrm{p}}) \quad \text{on} \quad \Sigma, \\ \mathbf{t}_{\mathrm{f}} \cdot \mathbf{n}_{\mathrm{f}} + c_1(\phi_{\mathrm{f}} - \phi_{\mathrm{p}})\phi_{\mathrm{f}} + c_{3,\mathrm{f}}\phi_{\mathrm{f}} = c_2\phi_{\mathrm{p}}, \quad \mathbf{t}_{\mathrm{p}} \cdot \mathbf{n}_{\mathrm{p}} + c_1(\phi_{\mathrm{p}} - \phi_{\mathrm{f}})\phi_{\mathrm{p}} + c_{3,\mathrm{p}}\phi_{\mathrm{p}} = c_2\phi_{\mathrm{f}} \quad \text{on} \quad \Sigma, \end{gathered} \tag{2.27}$$

where $c_{3,\mathrm{f}} = c_2 - c_0$ and $c_{3,\mathrm{p}} = c_2 + c_0$. In turn, since the membrane is defined only as $\partial\Omega_{\mathrm{f}} \cap \partial\Omega_{\mathrm{p}} = \Sigma$, we consider the following wall-boundary conditions

$$\mathbf{u}_\star = \mathbf{0} \quad \text{on} \quad \Gamma_{\mathrm{w},\star}, \quad \text{and} \quad \mathbf{t}_\star \cdot \mathbf{n}_\star = 0 \quad \text{on} \quad \Gamma_{\mathrm{w},\star}. \tag{2.28}$$

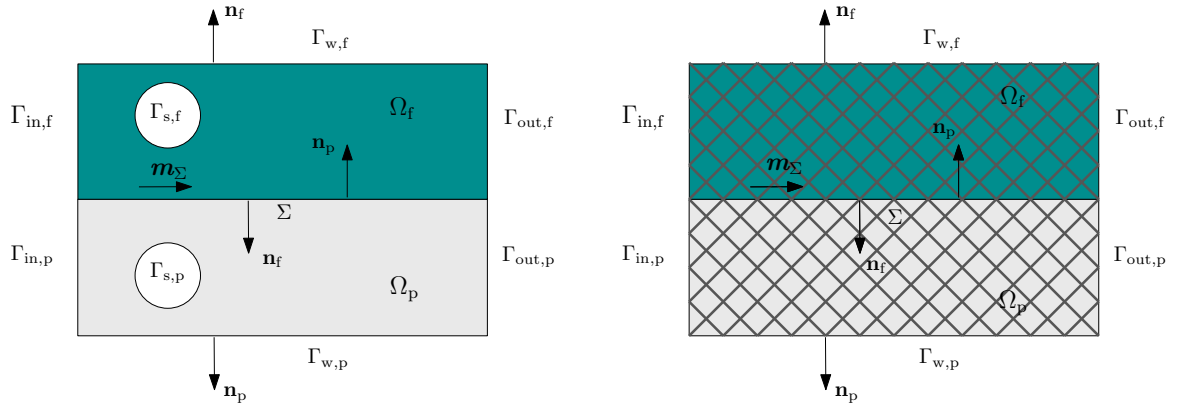

Figure 2.2: Sketch of the coupled feed and permeate channels. Explicit spacers (left) and implicit spacers (right).

2.2.1 Mixed finite element discretization and solving strategy.

Let $\mathcal{T}_h^{\mathrm{f}}$ and $\mathcal{T}_h^{\mathrm{p}}$ be the respective triangulations of the domains Ω_f and Ω_p formed by shape-regular triangles of diameter h_K and denote by h_f and h_p their corresponding meshsizes. Assume that they match on Σ so that $\mathcal{T}_h := \mathcal{T}_h^{\mathrm{f}} \cup \mathcal{T}_h^{\mathrm{p}}$ is a triangulation of Ω. Hereafter, $h := \max\{h_\mathrm{f}, h_\mathrm{p}\}$. Since this two channel model is originated by coupling two single channels, from (2.22) we can deduce that the block structure of the non linear system of equations is the following:

$$\left(\begin{array}{c|c|c|c} \mathcal{A}^{\mathrm{f}}_{\mathbf{S}}(\mathbf{u}_{\mathrm{f},h}) & \mathbf{0} & \mathbf{0} & \mathbf{0} \\ \hline \mathbf{0} & \mathcal{A}^{\mathrm{p}}_{\mathbf{S}}(\mathbf{u}_{\mathrm{p},h}) & \mathbf{0} & \mathbf{0} \\ \hline \mathbf{0} & \mathbf{0} & \mathcal{A}^{\mathrm{f}}_{\mathbf{T}}(\mathbf{u}_{\mathrm{f},h}, \xi_{h,\mathrm{f}} - \xi_{h,\mathrm{p}}) & \mathbf{0} \\ \hline \mathbf{0} & \mathbf{0} & \mathbf{0} & \mathcal{A}^{\mathrm{p}}_{\mathbf{T}}(\mathbf{u}_{\mathrm{p},h}, \xi_{h,\mathrm{p}} - \xi_{h,\mathrm{f}}) \end{array}\right) \left(\begin{array}{c} \mathbf{X}_\mathrm{f} \\ \mathbf{X}_\mathrm{p} \\ \mathbf{Y}_\mathrm{f} \\ \mathbf{Y}_\mathrm{p} \end{array}\right) = \left(\begin{array}{c} \mathbf{G}^{\mathrm{f}}(\xi_{\mathrm{f},h} - \xi_{\mathrm{p},h}) \\ \mathbf{G}^{\mathrm{p}}(\xi_{\mathrm{f},h} - \xi_{\mathrm{p},h}) \\ \mathcal{G}^{\mathrm{f}}(\xi_{\mathrm{p},h}) \\ \mathcal{G}^{\mathrm{p}}(\xi_{\mathrm{f},h}) \end{array}\right),$$

where for $\star \in \{\mathrm{f}, \mathrm{p}\}$, $\mathcal{A}^\star_{\mathbf{S}}(\mathbf{u}_{\star,h})$ and $\mathcal{A}^\star_{\mathbf{T}}(\mathbf{u}_{\star,h}, \chi_h)$ are defined exactly as in (2.23) and (2.24), respectively, considering in this case that the integrals and functions in the bilinear forms that induce these matrices (cf. (2.19)–(2.21)), take values in $\Omega_\star$. In addition, for each $\star \in \{\mathrm{f}, \mathrm{p}\}$:

$$\mathbf{X}_\star := (\boldsymbol{\sigma}_{\star,h}, \mathbf{u}_{\star,h})^t \in \mathbb{H}^\star_h \times \mathbf{Q}^\star_h \quad \text{and} \quad \mathbf{Y}_\star := (\mathbf{t}_{\star,h}, \phi_{\star,h}, \xi_{\star,h})^t \in \mathbf{H}^\star_h \times \mathrm{X}^\star_h \times \mathrm{M}^\star_h,$$

where $\mathbb{H}^\star_h$, $\mathbf{Q}^\star_h$, $\mathbf{H}^\star_h$, $\mathrm{X}^\star_h$ and $\mathrm{M}^\star_h$ are the discrete spaces introduced in (2.10) adapted to $\Omega_\star$. Also, $\mathcal{G}^\star$ and $\mathbf{G}^\star$ are given by

$$\mathcal{G}^{\mathrm{f}}(\xi_{\mathrm{p},h}) := (\mathbf{0}, \mathcal{F}^{\mathrm{f}}(\xi_{\mathrm{p},h}))^t, \quad \mathcal{G}^{\mathrm{p}}(\xi_{\mathrm{f},h}) := (\mathbf{0}, \mathcal{F}^{\mathrm{p}}(\xi_{\mathrm{f},h}))^t \quad \text{and} \quad \mathbf{G}^\star(\xi_{\mathrm{f},h} - \xi_{\mathrm{p},h}) := (\mathbf{F}^\star_{\mathsf{c}}(\xi_{\mathrm{f},h} - \xi_{\mathrm{p},h}), \mathbf{0})^t.$$

Here, $\mathbf{F}^\star_{\mathsf{c}}(\xi_{\mathrm{f},h} - \xi_{\mathrm{p},h})$ is the vector associated to the functional that involves the Dirichlet boundary condition, defined as $\mathbf{F}^\star_{\mathsf{c}}(\xi_{\mathrm{f},h} - \xi_{\mathrm{p},h}; \boldsymbol{\tau}_{\star,h}) := \displaystyle\int_{\Gamma^{\mathrm{c}}_{\mathrm{out},\star}} (\boldsymbol{\tau}_{\star,h}\mathbf{n}_\star) \cdot \mathbf{u}_{\mathrm{D},\,\xi_{\mathrm{f},h} - \xi_{\mathrm{p},h}}$, where

$$\mathbf{u}^\star_{\mathrm{D},\,\xi_{\mathrm{f},h} - \xi_{\mathrm{p},h}} = \mathbf{u}_\star|_{\Gamma^{\mathrm{c}}_{\mathrm{out},\star}} = \left\{ \begin{array}{lll} \mathbf{0} & \text{on} & \Gamma_{\mathrm{w},\star}, \\ \mathbf{u}_{\mathrm{in},\star} & \text{on} & \Gamma_{\mathrm{in},\star}, \\ c_1(\xi_{\mathrm{f},h} - \xi_{\mathrm{p},h} + c_0)\mathbf{n}_\mathrm{f} & \text{on} & \Sigma, \end{array} \right. \tag{2.29}$$

with $\star \in \{\mathrm{f}, \mathrm{p}\}$. Moreover, $\mathcal{F}^{\mathrm{f}}(\xi_{\mathrm{p},h})$ and $\mathcal{F}^{\mathrm{p}}(\xi_{\mathrm{f},h})$ are the vectors associated to the functionals that arise from coupling terms in (2.27), given by

$$\mathcal{F}^{\mathrm{f}}(\xi_{\mathrm{p},h}; \eta_{\mathrm{f},h}) := -c_2 \int_\Sigma \xi_{\mathrm{p},h}\, \eta_{\mathrm{f},h} \quad \text{and} \quad \mathcal{F}^{\mathrm{p}}(\xi_{\mathrm{f},h}; \eta_{\mathrm{p},h}) := -c_2 \int_\Sigma \xi_{\mathrm{f},h}\, \eta_{\mathrm{p},h}, \tag{2.30}$$

respectively. Finally, the resulting fixed point algorithm is similar to that of Section 2.1.2. Indeed, given $\xi^{n-1}_{\star,h}$ and $\mathbf{u}^{n-1}_{\star,h}$, we look for $\mathbf{X}^n_\star := (\boldsymbol{\sigma}^n_{\star,h}, \mathbf{u}^n_{\star,h})^t$, with $\star \in \{\mathrm{f}, \mathrm{p}\}$, such that

$$\left(\begin{array}{c|c} \mathcal{A}^{\mathrm{f}}_{\mathbf{S}}(\mathbf{u}^{n-1}_{\mathrm{f},h}) & \mathbf{0} \\ \hline \mathbf{0} & \mathcal{A}^{\mathrm{p}}_{\mathbf{S}}(\mathbf{u}^{n-1}_{\mathrm{p},h}) \end{array}\right) \left(\begin{array}{c} \mathbf{X}^n_\mathrm{f} \\ \mathbf{X}^n_\mathrm{p} \end{array}\right) = \left(\begin{array}{c} \mathbf{G}^{\mathrm{f}}(\xi^n_{\mathrm{f},h} - \xi^n_{\mathrm{p},h}) \\ \mathbf{G}^{\mathrm{p}}(\xi^n_{\mathrm{f},h} - \xi^n_{\mathrm{p},h}) \end{array}\right).$$

Then, after $\mathbf{X}_\star^n := (\boldsymbol{\sigma}_{\star,h}^n, \mathbf{u}_{\star,h}^n)^t$ is computed, we find for $\mathbf{Y}_\star^n := (\mathbf{t}_{\star,h}^n, \phi_{\star,h}^n, \xi_{h,\star}^n)^t$, with $\star \in \{\mathrm{f}, \mathrm{p}\}$, such that

$$\left(\begin{array}{c|c} \mathcal{A}_{\mathbf{T}}^{\mathrm{f}}(\mathbf{u}_{\mathrm{f},h}^n, \xi_{h,\mathrm{f}}^{n-1} - \xi_{h,\mathrm{p}}^{n-1}) & \mathbf{0} \\ \hline \mathbf{0} & \mathcal{A}_{\mathbf{T}}^{\mathrm{p}}(\mathbf{u}_{\mathrm{p},h}^n, \xi_{h,\mathrm{p}}^{n-1} - \xi_{h,\mathrm{f}}^{n-1}) \end{array}\right) \begin{pmatrix} \mathbf{Y}_{\mathrm{f}}^n \\ \mathbf{Y}_{\mathrm{p}}^n \end{pmatrix} = \begin{pmatrix} \mathcal{G}^{\mathrm{f}}(\xi_{\mathrm{p},h}^{n-1}) \\ \mathcal{G}^{\mathrm{p}}(\xi_{\mathrm{f},h}^{n-1}) \end{pmatrix}.$$

3 Numerical simulations

We now turn to the computational results to illustrate a variety of examples related to the RO process in both single and coupled channel systems, and considering explicit and implicit spacers. The computational implementation is based on a `FreeFem++` code (cf. [15]) and the use of the direct linear solvers UMFPACK (cf. [10]). The iterative method comes straightforward from the uncoupling strategy presented in Sections 2.1.2 and 2.2.1 and the iterations are terminated once the relative error of the entire coefficient vectors between two consecutive iterates is sufficiently small, that is

$$\frac{\|\mathbf{coeff}^{m+1} - \mathbf{coeff}^{m}\|_{l^2}}{\|\mathbf{coeff}^{m+1}\|_{l^2}} \leqslant \mathtt{tol}\,,$$

where $\|\cdot\|_{l^2}$ stands for the usual Euclidean norm in $\mathbb{R}^{\mathtt{dof}}$, with `dof` denoting the total number of degrees of freedom defining the finite element subspaces $\mathbb{H}_h$, $\mathbf{Q}_h$, $\mathbf{H}_h$, X_h, and M_h, when considering a single channel, and $\mathbb{H}_h^\star$, $\mathbf{Q}_h^\star$, $\mathbf{H}_h^\star$, $\mathrm{X}_h^\star$ and $\mathrm{M}_h^\star$, with $\star \in \{\mathrm{f}, \mathrm{p}\}$ for the case of two channels. In this way, the global physical parameters specified in Section 2.1 are taken in Table 3.1 [8, 28].

Parameter	Meaning	Value	Units
T	System temperature	298	K
R	Ideal gas constant	8.314	$Jmol^{-1}K^{-1}$
i	Number of ions from salt solution	2	$-$
ΔP	Hydrostatic transmembrane pressure	$\Delta P_1 := 4053000$ $\Delta P_2 := 5575875$	Pa
ρ	Feed/permeate fluid density	1027.2	$kg\,m^{-3}$
κ	Feed/permeate diffusivity of salt in water	1.611×10^{-9}	$m^2 s^{-1}$
ν	Feed/permeate fluid dynamic viscosity	8.9×10^{-4}	$kg\,m^{-1}s^{-1}$
A	Membrane water permeability	2.5×10^{-12}	$ms^{-1}\,Pa^{-1}$
B	Membrane salt permeability	2.5×10^{-8}	$m\,s^{-1}$

Table 3.1: global physical parameters

3.1 A single feed channel.

We consider the computational domain $\Omega = (0, L) \times (0, d)$, where $L = 15\,mm$ and $d = 0.74\,mm$. In turn, the inlet velocity profile is set as follows

$$\mathbf{u}_{\mathrm{in}} := \left(6\mathrm{u}_{\mathrm{in}}\frac{y}{d}\left(1 - \frac{y}{d}\right), 2(c_0 - c_1\phi_{\mathrm{in}})\frac{y}{d} - (c_0 - c_1\phi_{\mathrm{in}})\right)^t, \quad y \in [0, d], \tag{3.1}$$

where $\mathrm{u}_{\mathrm{in,f}}$ stands for the inlet mean feed fluid velocity.

Simulation 1. A feed channel with no salt concentration. We consider a channel without explicit spacers and the numerical method is tested against classic analytical models of momentum transport in membrane modules, that is, those of Poiseuille and Berman flow models, by comparison of the pressure drop, denoted by $\Delta p := p(0, d/2) - p(x, d/2)$. This validation implies the simulation of a uniform permeation of pure solvent ($\phi_{\mathrm{f}} = 0$), and then the pressure drop is obtained by solving the equations of motion with the following boundary conditions

$$\mathbf{u} \cdot \mathbf{n} = c_0 \text{ (for Berman flow)} \quad \text{on} \quad \Sigma \quad \text{and} \quad \mathbf{u} \cdot \mathbf{n} = 0 \text{ (for Poiseuille flow)} \quad \text{on} \quad \Sigma.$$

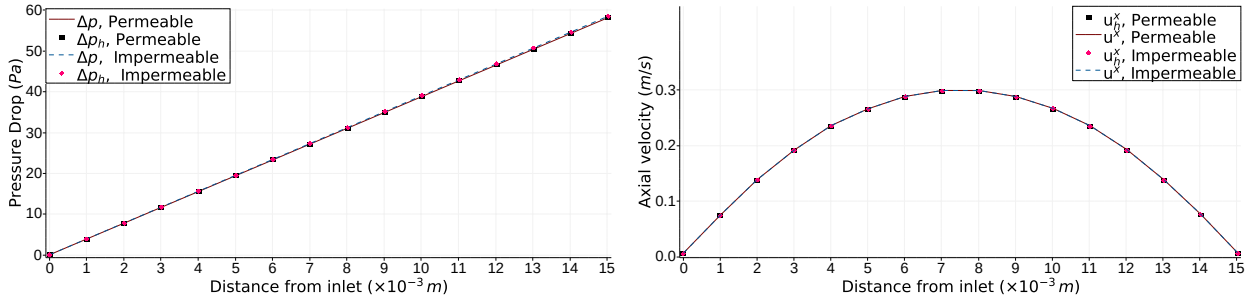

Figure 3.1: Comparison of exact vs. approximate pressure drop (left) and axial velocity (right) for a single channel. Simulation conditions: $\mathrm{u_{in}} = 0.2\,m/s$, $\Delta P = \Delta P_2$ and clean water, for Poiseuille (impermeable) and Berman (permeable) flows.

We recall that for the Poiseuille flow the boundary condition on the membrane means that $A = 0$ (impermeable walls). In the case of Berman flow model, we have the following exact pressure drop equation

$$\Delta p(x, d/2) := \Big(\frac{1}{2}\rho \mathrm{u}_{\mathrm{in}}^2\Big)\Big(\frac{24}{Re} - \frac{648}{35}\frac{Re_{\mathbf{n}}}{Re}\Big)\Big(1 - \frac{2Re_{\mathbf{n}}x}{Re\,d}\Big)\Big(\frac{2x}{d}\Big), \tag{3.2}$$

where $Re := \dfrac{2\,\rho\,d\,\mathrm{u}_{\mathrm{in}}}{\nu}$ is the cross flow Reynolds number, and $Re_{\mathbf{n}} := \dfrac{\rho\,d\,(\mathbf{u}\cdot\mathbf{n})}{2\,\nu}$ is the Reynolds number at the channel walls. We note that the reduced pressure drop for the Poiseuille flow is obtained using the fact that $Re_{\mathbf{n}} = 0$, that is

$$\Delta p(x, d/2) := \Big(\frac{1}{2}\rho_{\mathrm{f}} \mathrm{u}_{\mathrm{in}}^2\Big)\Big(\frac{24}{Re}\Big)\Big(\frac{2x}{d}\Big). \tag{3.3}$$

We simulate the case where $\mathrm{u_{in}} = 0.2m/s$ and $\Delta P = \Delta P_2$. Figure 3.1 (left) shows the analytical pressure drop predicted by the equation (3.2), compared with the discrete pressure drop, denoted by $\Delta p_h(x, d/2)$. We observe that our mixed finite element model accurately captures the axial pressure drops for both, the permeable and impermeable walls. In addtion, in Figure 3.1 (right) we plot the axial velocity along the segment starting at $(0, 0)$ and ending at (L, d). We observe that the numerical approximation agrees with the exact solution given by (3.1). We would like to remark that even though the analytical solution obtained by Berman [4], does not consider the boundary condition (2.2) at the outlet, it is commonly used to validate the numerical simulations [8, 28]. Since the channel is sufficiently long, the effect of the outlet boundary condition in the behaviour of the solution will be negligible away from the outlet.

Simulation 2. A feed channel with salt concentration with explicit and implicit spacers. We now employ our numerical method to compare the behaviour of the system considering three different cases: (S.1) channel without spacers, (S.2) with explicit submerged spacers and (S.3) implicit spacers. For a single channel with a constant inlet salt concentration of $\phi_{\mathrm{in}} = 600\,\frac{mol}{m^3}$, varying the inlet mean feed fluid velocities $\mathrm{u_{in}} \in \{0.1m/s, 0.2m/s\}$, and $\Delta P \in \{\Delta P_1, \Delta P_2\}$, we perform a total of twelve scenarios. Also, for the cases (S.2) and (S.3), we consider a number of spacers $\mathtt{N_{sp}} = 3$ of diameter $d_{\mathrm{s}} = 0.36\,mm$. In particular, the spacers for (S.2) centered at $(L/4, d/2), (L/2, d/2)$ and $(3L/4, d/2)$. In addition for (S.3), taking into account that the sphericity of the particles is $\Phi = 1$, we find that the porosity of the medium and the porous medium permeability become $\varepsilon = 0.97249$ and $\widehat{K} = 8.74987 \times 10^{-7}\,m^2$, respectively. Consequently, the resulting Darcy and Forchheimer coefficients are $\widehat{\mathtt{D}} = 1.01716 \times 10^3\,\frac{kg}{sm^3}$ and $\widehat{\mathtt{F}} = 1.59112 \times 10^5\,\frac{kg}{m^4}$, respectively. Darcy's coefficient gives a linear relationship between the pressure drop and the velocity of the fluid, its value depends on physicochemical parameters such as the permeability and viscosity of the medium. For values of the Darcy number ($\mathtt{Da} = \widehat{K}/d^2$) above 10^{-3} (in our case $\mathtt{Da} = 1.59$), an additional term is needed to account for nonlinear effects between pressure drop and velocity [20]. These are attributed to the insurgence of inertial effects within the laminar flow regime. For these nonlinear relationship we use the Forchheimer term, which is proportional to the fluid density and to the second power of the flow rate [5].

As is usual in this type of simulations, and with the end of avoiding potential errors due to improper meshing, we employ our mixed method scheme combined to a high resolution mesh near the interface. This approach has been demonstrated to be crucial for achieving optimal results [16, 28].

Discussion. Representative velocity profiles (left), concentration fields (middle), and pressure drops (right) are shown in Figure 3.2. In an empty RO feed channel (case (S.1)), the parabolic velocity profile is preserved along the entire region. Similar results are observed for the porous cases (S.3), but as expected, the value of the axial velocity profile is slightly smaller than the one of case (S.1). In fact, for an empty channel there is not any material affecting the fluid flow allowing higher velocities in comparison with a porous channel where the fluid passes through spaces between small obstacles. On the other hand, as shown in the center panel of Figure 3.2 (case (S.2)), a submerged spacer produces an increment in the fluid velocity in the region surrounding the spacer. As a consequence, we observe abrupt changes in the pressure drop for the submerged configuration (case (S.2) in Figure 3.2) in the whole transversal section near the spacer, which is commonly attributed to be momentum losses due to the changes in the flow direction. Here, we also observe a pressure drop in the case (S.3) because the effect of the spacers is been distributed as a porous medium. On the other hand, we note that the empty channel produces a thicker salt concentration layer compared to the others, this is because the submerged spacers have a local thinning effect on the salt layer. In turn, the same effect is produced by the porous channel but in a distributed way. To see this effect more clearly in Figure 3.3 we display the concentration along the vertical line at $x = 7.7mm$, $y \in [0, 0.1]\,mm$, for the three cases. We recall that a circular spacer of diameter $d_s = 0.36\,mm$ and centered at the point $(7.5\,mm, 0.37\,mm)$ is placed in the channel. Then, the segment $x = 7.7\,mm$ is located immediately $0.02\,mm$ at the right of the circular obstacle with the goal of observing the effect of the spacer in the concentration. As expected, the concentration of salt is higher near the membrane. We also notice that the values of the concentration and thickness of the salt layer decrease when the inlet velocity increases while maintaining a fixed hydrostatic transmembrane pressure, which in turn leads to a higher permeate velocity (see Figures 3.4 and 3.5). In turn, the concentration increases when the hydrostatic transmembrane pressure increases. On the other hand, the concentration in the empty channel (case (S.1)) is higher compared to cases (S.2) and (S.3). In other words, the presence of explicit or implicit spacers lowers the salt concentration near the membrane. Moreover, the concentration in case (S.3) is higher that in case (S.2) due to the local effect of the spacer, as we can observe in the bottom panels of Figures 3.4 and 3.5. Here, for the case (S.2), we observe three local minima when the distance from the inlet is approximately $3.75\,mm$, $7.5\,mm$ and $11.25\,mm$, respectively. This values correspond to the horizontal component the center of each circular spacers.

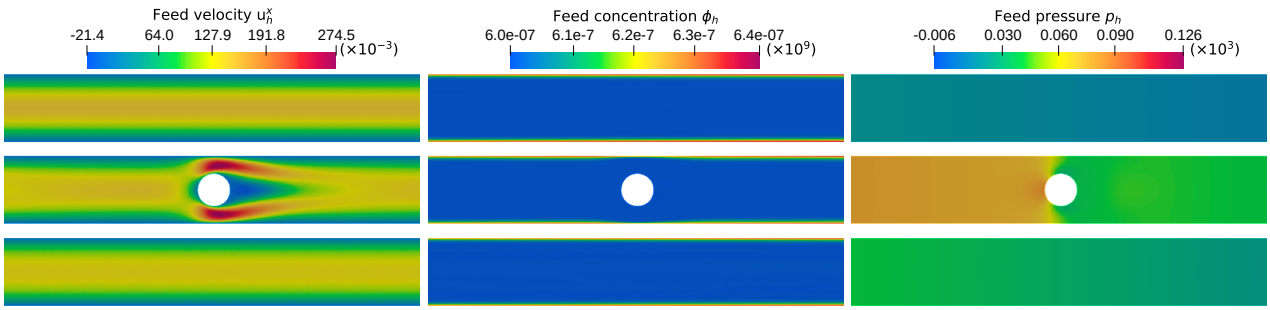

Figure 3.2: Zoom in the region $[5, 10]\,mm \times [0, 0.74]\,mm$. From left to right: axial velocity profiles (left), concentration fields (middle), and pressure drops (right). From top to bottom, cases (S.1), (S.2) and (S.3). Simulation conditions: $u_{in} = 0.1\,m/s$, $\Delta P = \Delta P_1$.

Now, looking at the plots in Figures 3.4 and 3.5, we observe that for each case ((S.1), (S.2) or (S.3)), the hydrostatic transmembrane pressure $\Delta P = \Delta P_1$ (top-left panel) and $\Delta P = \Delta P_2$ (top-right panel), has no influence on the pressure drop. Nevertheless, its increment produces a higher permeate velocity flow, as we can see in the middle panels, yielding an inlet permeation velocity of $2.69 \times 10^{-6}\,m/s$ and $6.50 \times 10^{-6}\,m/s$, for ΔP_1 and ΔP_2, respectively. If the transmembrane pressure were even higher we could observe a subtle decrease in the pressure drop, since there would be more permeate flow and less velocity gradients near the bottleneck formed at the spacers. However, the permeate velocity is 6 orders of magnitude lower than the inlet flow, so it is not possible to evidence this phenomenon. For the same reason we can say that the transmembrane pressure does not have a major impact on the hydrodynamics of the channel [8]. In turn, the increment of ΔP has as a consequence in a higher salt concentration (bottom panels) on the membrane.

Next, we focus on analyzing comparatively the three proposed configurations. We observe in the empty channel (S.1) that the salt concentration (bottom panels) at the membrane is monotonically increasing with respect to the distance from the inlet, which means a higher salt concentration as the fluid passes through the

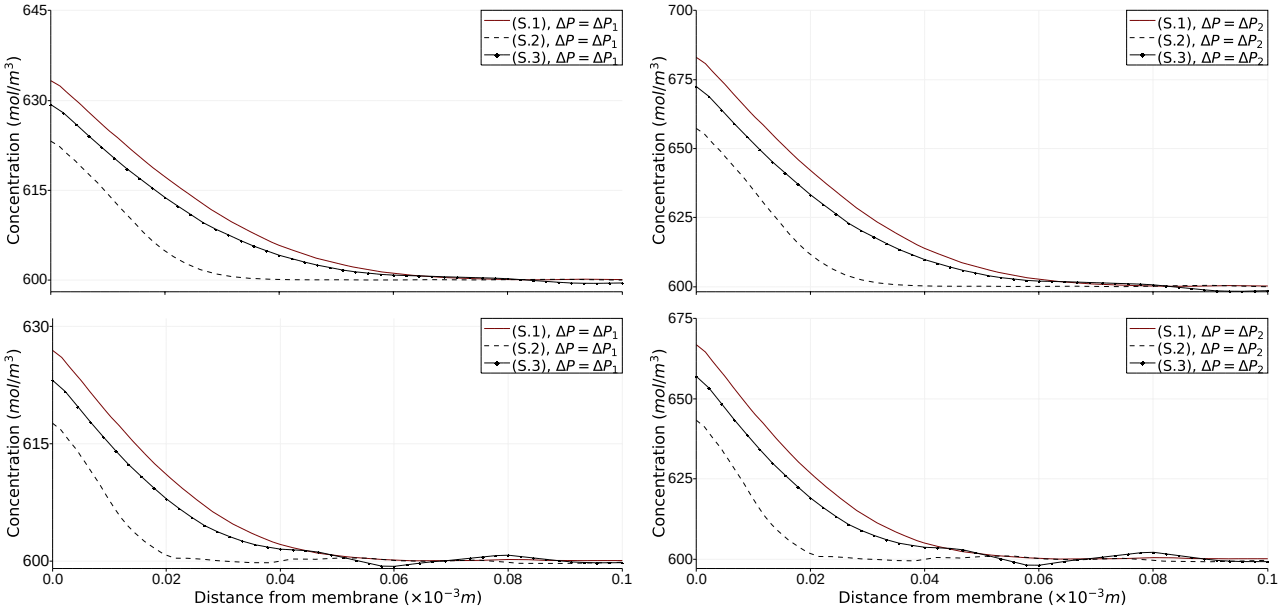

Figure 3.3: Salt concentration along the vertical line at $x = 7.7\,mm$, $y \in [0, 0.1]\,mm$ for the three cases (S.1), (S.2) and (S.3). Simulation conditions: u_{in} equal to $0.1\,m/s$ (top panels) and $0.2\,m/s$ (bottom panels); and ΔP equal to ΔP_1 (left panels) and ΔP_2 (right panels).

membrane. This implies a lower permeate velocity (center panels). In this way, the spacers in the feed channel play a key roll since they generally enhance mixing, reduce (rejected) solute concentration and increase in permeate production (total permeate flow per unit length $\dot{V}/W$, to be defined below) compared to the absence of spacers, as demonstrated in previous works [1, 18, 28]. Within the limits of the current study, for the single channel with two permeable walls, we consider the particular case of submerged spacers (case (S.2)), since it has been shown to exhibit the highest permeate production compared to cavity and zig-zag spacers [8]. If we compare the cases (S.1) and (S.2) in Figures 3.4 and 3.5, we observe that not only the values of the salt concentration in (S.2) are lower than those of (S.1) throughout the regions influenced by the spacers, but also the former are lower than the latter in the regions between the spacers, under the same operating conditions. In addition, we know that the concentration has a direct effect on the permeate velocity (see second equation in (2.3)). This fact, is also confirmed in our simulations (middle and bottom panels of Figures 3.4 and 3.5), where the behaviour of the permeate velocity and concentration is opposite.

On the other hand, as we mentioned before, case (S.3) consists of emulating the spacer-filled channel as a porous medium, where its porosity is calculated by distributing in the entire channel the effect of the spacer. As a consequence, the model will no detect the local effect. Instead, as we can see in Figures 3.4 and 3.5, the black lines show a global behaviour of the variables. In addition, as we mentioned before, an increment in the inlet mass flow while maintaining a fixed hydrostatic transmembrane pressure, reduces the concentration at the membrane, leading to a higher permeate velocity and larger pressure losses (higher energy cost). In fact, the pressure drop is an unavoidable phenomenon along the entire channel, being the empty channel case (S.1) the one with the lowest pressure drop, whereas the case (S.2) exhibits a larger pressure drop, due to the presence of submerged spacers.

Now, to measure the impact of each case on permeate production, we compute the total volumetric flow per unit width. The channel in Figure 2.1, is actually a cross section of the region $[0, L] \times [0, d] \times [0, W]$, for a positive width W. Then, we utilize the following definition of the volumetric flow from the flux:

$$\frac{\dot{V}}{W} = \int_{\Sigma} |\mathbf{u}_h(s) \cdot \mathbf{n}| ds, \tag{3.4}$$

where $\dot{V}$ is the total volumetric flow of the permeate from the membrane walls and we recall that $\mathbf{u}_h(s) \cdot \mathbf{n}$ is the approximation of the permeate flux at a distance s from the inlet, obtained by our numerical scheme. In the simulations W is taken to be equal to L.

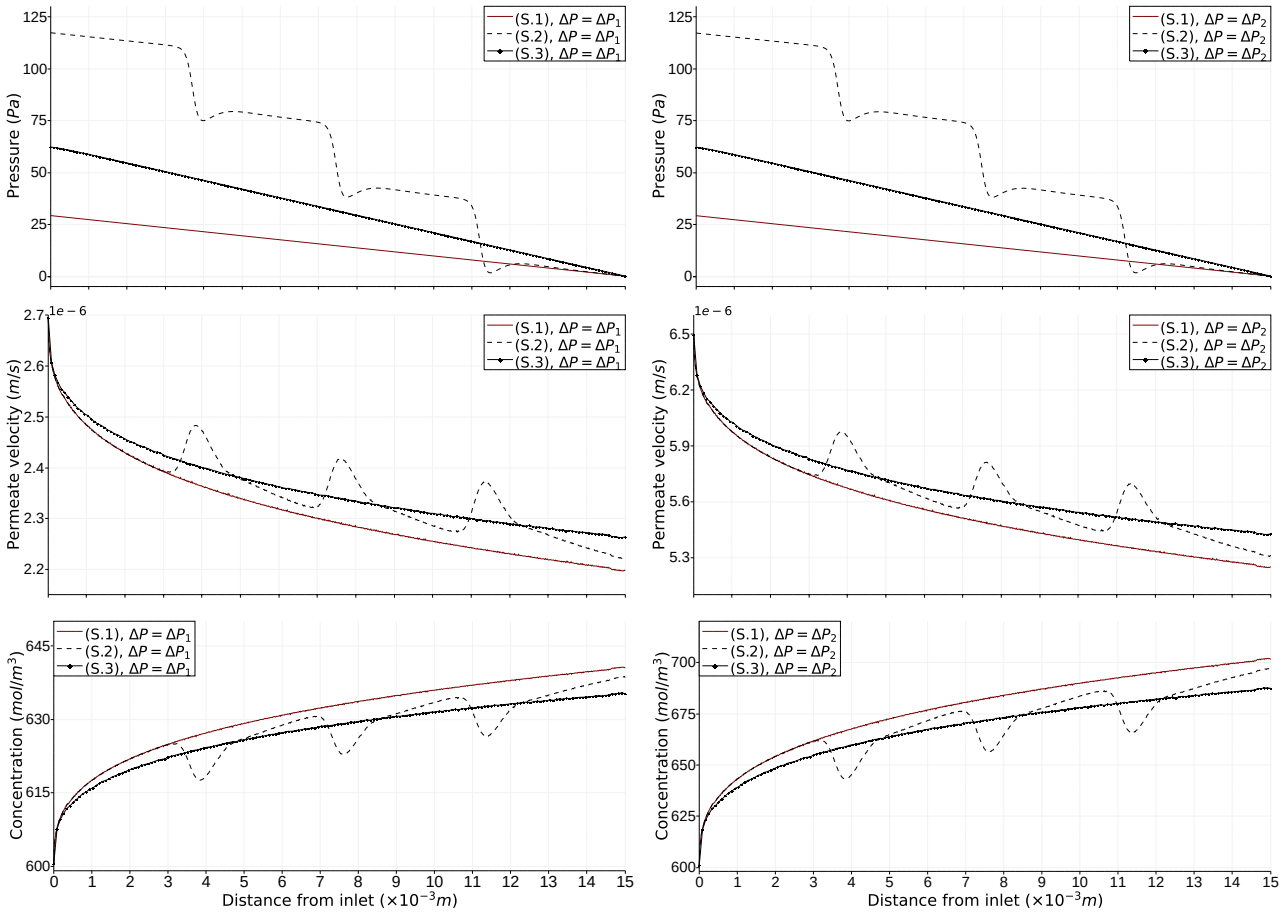

Figure 3.4: Relative pressure drop (top panels), permeate velocity (middle) and concentration level (bottom panels) at the membrane $y = 0\,mm$ without spacers (S.1), with submerged explicit spacers (S.2), and implicit spacers (S.3). Simulation conditions: $\mathrm{u_{in}} = 0.1\,m/s$; and ΔP equal to ΔP_1 (left panels) and ΔP_2 (right panels).

We report the values of $\dot{V}/W$ obtained in different scenarios in Table 3.2. The results show differences up to 2.5 times comparing the lowest ($\mathrm{u_{in}} = 0.1\,m/s$, $\Delta P = \Delta P_1$, case (S.1)) and the highest ($\mathrm{u_{in}} = 0.2\,m/s$, $\Delta P = \Delta P_2$, case (S.3)) permeate production values. In turn, Table 3.3 shows the increment ($\rightarrow$) rate of the values of the permeate production $\dot{V}/W$ reported in Table 3.2. For example, the third row and second column reads as follows: A simulation considering $\mathrm{u_{in}} = 0.1\,m/s$ and case (S.2) produces an increment of 139.56% when varying ΔP from ΔP_1 by ΔP_2. It is worth noting that the largest differences in the permeate production are due to the increment in the hydrostatic transmembrane pressure for all configurations, as we observe in the second and third row of Table 3.3. However, it is important to bear in mind that this leads to an increment in the concentration on the membrane. As a Consequence, we would need to increase the inlet velocity to remove the salt near the membrane, but this leads to a higher pressure drop (energy loss), as we have observed in Figures 3.4 and 3.5. In other words in order to determine the optimal values of all the parameters, we need to employ a constrained optimization algorithm and further numerical investigations will be carried out in a future work.

Finally, we compare how well the porous medium model (case (S.3)) emulate the case of submerged explicit spacers (S.2). In Table 3.3 (last column, fifth to eight rows), we observe that the case (S.3), in a very rough sense, differs from (S.2) only between 0.16% and 0.26% of the total permeate flow. This means, as we know, that considering implicit spacers allow us to predict a global behaviour with lower computational cost compared to the case of explicit spacers.

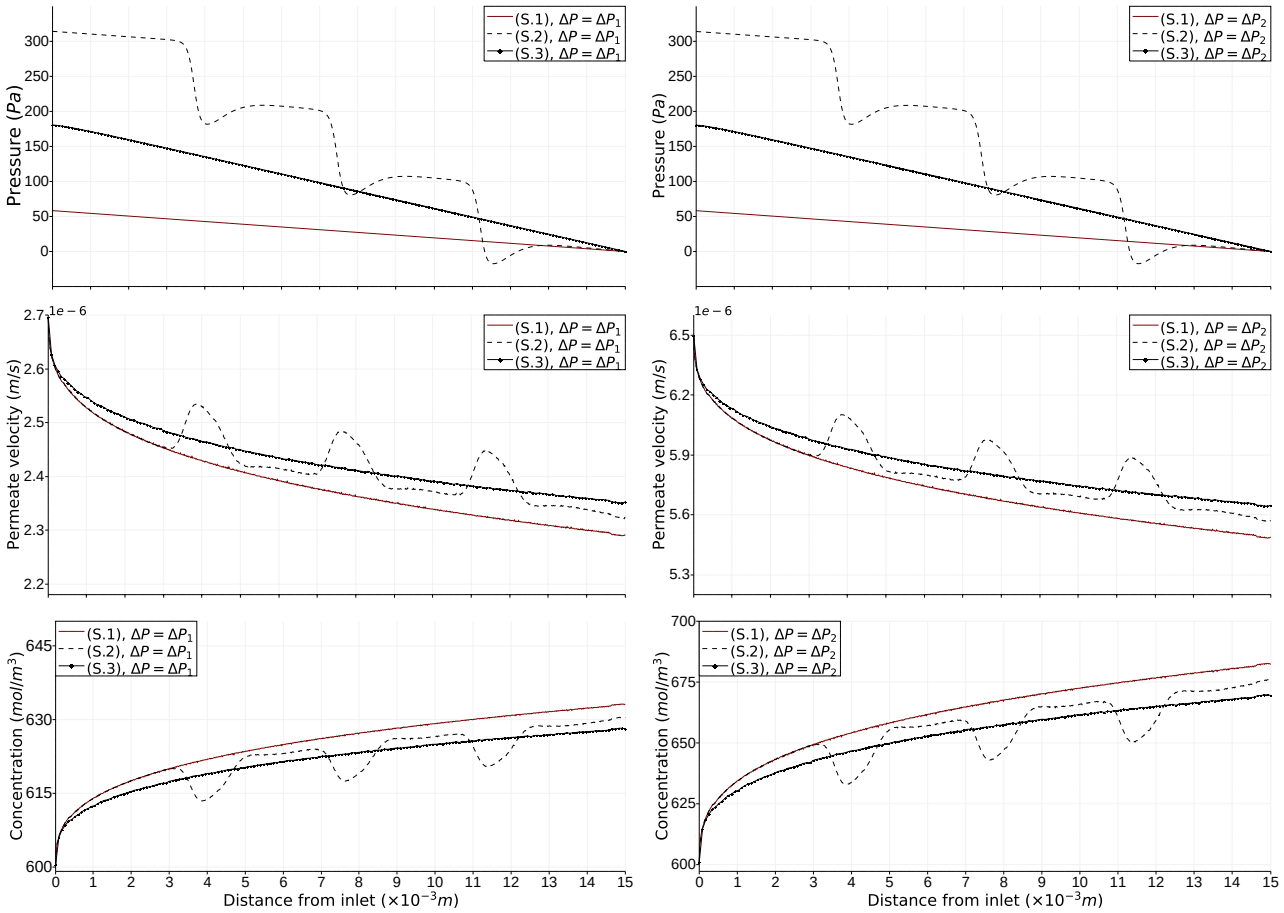

Figure 3.5: Same as Figure 3.4 but considering $\mathrm{u_{in}} = 0.2\,m/s$.

	$\Delta P = \Delta P_1$		$\Delta P = \Delta P_2$	
case	$\mathrm{u_{in}}$ (m/s)	$\dot{V}/W$ (m^2/s)	$\mathrm{u_{in}}$ (m/s)	$\dot{V}/W$ (m^2/s)
(S.1)	0.1	6.92222×10^{-8}	0.1	1.65829×10^{-7}
	0.2	7.14278×10^{-8}	0.2	1.71444×10^{-7}
(S.2)	0.1	7.04797×10^{-8}	0.1	1.69034×10^{-7}
	0.2	7.26112×10^{-8}	0.2	1.74439×10^{-7}
(S.3)	0.1	7.05906×10^{-8}	0.1	1.69470×10^{-7}
	0.2	7.27309×10^{-8}	0.2	1.74816×10^{-7}

Table 3.2: Total permeate flow per unit length $\dot{V}/W$ in a single channel for different values of $\mathrm{u_{in}}$ and ΔP, of the three cases (S.1), (S.2) and (S.3).

3.2 Coupled feed and permeate channel.

We also consider $L = 15\,mm$ and $d = 0.74\,mm$, and the computational domain $\Omega = \Omega_\mathrm{f} \cup \Omega_\mathrm{p} \cup \Sigma$, where $\Omega_\mathrm{f} = (0, L) \times (d, 2d)$, $\Omega_\mathrm{p} = (0, L) \times (0, d)$, and $\Sigma = (0, L) \times \{d\}$. Here, we consider the inlet velocity profiles of the feed and permeate channels as

$$\begin{aligned} \mathbf{u}_{\mathrm{in,f}} &:= \left(6\mathrm{u}_{\mathrm{in,f}}\left(1-\frac{y}{d}\right)\left(\frac{y}{d}-2\right), (c_0 - c_1(\phi_{\mathrm{in,f}} - \phi_{\mathrm{in,p}}))\left(\frac{y}{d}-2\right)\right)^t, \quad y \in [d, 2d], \\ \mathbf{u}_{\mathrm{in,p}} &:= \left(6\mathrm{u}_{\mathrm{in,p}}\frac{y}{d}\left(1-\frac{y}{d}\right), -(c_0 - c_1(\phi_{\mathrm{in,f}} - \phi_{\mathrm{in,p}}))\frac{y}{d}\right)^t, \quad y \in [0, d], \end{aligned} \tag{3.5}$$

respectively, where $\mathrm{u_{in,f}}$ and $\mathrm{u_{in,p}}$ stand for the inlet mean feed and permeate fluid velocities, respectively.

ΔP_1−(S.1): $0.1\,m/s \xrightarrow{3.19\%} 0.2\,m/s$	ΔP_1−(S.2): $0.1\,m/s \xrightarrow{3.02\%} 0.2\,m/s$	ΔP_1− (S.3): $0.1\,m/s \xrightarrow{3.03\%} 0.2\,m/s$
ΔP_2−(S.1): $0.1\,m/s \xrightarrow{3.39\%} 0.2\,m/s$	ΔP_2−(S.2): $0.1\,m/s \xrightarrow{3.20\%} 0.2\,m/s$	ΔP_2−(S.3): $0.1\,m/s \xrightarrow{3.15\%} 0.2\,m/s$
$0.1\,m/s$−(S.1): $\Delta P_1 \xrightarrow{139.56\%} \Delta P_2$	$0.1\,m/s$−(S.2): $\Delta P_1 \xrightarrow{139.83\%} \Delta P_2$	$0.1\,m/s$−(S.3): $\Delta P_1 \xrightarrow{140.07\%} \Delta P_2$
$0.2\,m/s$−(S.1): $\Delta P_1 \xrightarrow{140.02\%} \Delta P_2$	$0.2\,m/s$−(S.2): $\Delta P_1 \xrightarrow{140.24\%} \Delta P_2$	$0.2\,m/s$−(S.3): $\Delta P_1 \xrightarrow{140.36\%} \Delta P_2$
$0.1\,m/s - \Delta P_1$: (S.1) $\xrightarrow{1.82\%}$ (S.2)	$0.1\,m/s - \Delta P_1$: (S.1) $\xrightarrow{1.98\%}$ (S.3)	$0.1\,m/s - \Delta P_1$: (S.2) $\xrightarrow{0.16\%}$ (S.3)
$0.2\,m/s - \Delta P_1$: (S.1) $\xrightarrow{1.66\%}$ (S.2)	$0.2\,m/s - \Delta P_1$: (S.1) $\xrightarrow{1.82\%}$ (S.3)	$0.2\,m/s - \Delta P_1$: (S.2) $\xrightarrow{0.16\%}$ (S.3)
$0.1\,m/s - \Delta P_2$: (S.1) $\xrightarrow{1.93\%}$ (S.2)	$0.1\,m/s - \Delta P_2$: (S.1) $\xrightarrow{2.20\%}$ (S.3)	$0.1\,m/s - \Delta P_2$: (S.2) $\xrightarrow{0.26\%}$ (S.3)
$0.2\,m/s - \Delta P_2$: (S.1) $\xrightarrow{1.75\%}$ (S.2)	$0.2\,m/s - \Delta P_2$: (S.1) $\xrightarrow{1.97\%}$ (S.3)	$0.2\,m/s - \Delta P_2$: (S.2) $\xrightarrow{0.22\%}$ (S.3)

Table 3.3: Increment rate in the value of $\dot{V}/W$ reported in Table 3.2, with respect to the variation of the velocity (first and second rows), hydrostatic transmembrane pressure (third and fourth rows) and configurations (fifth to eight rows).

Simulation 3. Coupled feed and permeate channel with salt concentration with explicit and implicit spacers. We now investigate the behaviour of the system that consists of a feed channel coupled to the permeate channel where the interface is the membrane. We consider five different cases: (C.1) channels without spacers, (C.2) with submerged spacers, (C.3) with zig-zag distributed spacers, (C.4) with cavity spacers, and (C.5) implicit spacers. We set a constant inlet salt concentration of $\phi_{\text{in,f}} = 600\,\frac{mol}{m^3}$ and $\phi_{\text{in,p}} = 6\,\frac{mol}{m^3}$, for the feed and permeate channels, respectively. For this analysis, we focus exclusively on the scenario where $\Delta P = \Delta P_2$, motivated by the fact that higher values of the hydrostatic transmembrane pressure produces a higher permeate production. The inlet mean feed and permeate fluid velocities are set as $0.1\,m/s$ and $0.01\,m/s$, respectively. Furthermore, we maintain three spacers for each channel of diameter $0.36\,mm$ with centers located according to Table 3.4.

	(C.2)	(C.3)	(C.4)
Feed channel	$\left(\frac{L}{4}, \frac{3d}{2}\right)$, $\left(\frac{L}{2}, \frac{3d}{2}\right)$, $\left(\frac{3L}{4}, \frac{3d}{2}\right)$.	$\left(\frac{L}{4}, \frac{5d}{4}\right)$, $\left(\frac{L}{2}, \frac{5d}{4}\right)$, $\left(\frac{3L}{4}, \frac{5d}{4}\right)$.	$\left(\frac{L}{4}, \frac{5d}{4}\right)$, $\left(\frac{L}{2}, \frac{7d}{4}\right)$, $\left(\frac{3L}{4}, \frac{5d}{4}\right)$.
Permeate channel	$\left(\frac{L}{4}, \frac{d}{2}\right)$, $\left(\frac{L}{2}, \frac{d}{2}\right)$, $\left(\frac{3L}{4}, \frac{d}{2}\right)$.	$\left(\frac{L}{4}, \frac{d}{4}\right)$, $\left(\frac{L}{2}, \frac{d}{4}\right)$, $\left(\frac{3L}{4}, \frac{d}{4}\right)$.	$\left(\frac{L}{4}, \frac{d}{4}\right)$, $\left(\frac{L}{2}, \frac{3d}{4}\right)$, $\left(\frac{3L}{4}, \frac{d}{4}\right)$.

Table 3.4: Coordinates of the center of the circular spacers located inside the feed and permeate channels.

Discussion. Velocity profiles in both, feed and permeate channels, for all cases are depicted in Figure 3.6. The axial velocity in cases (C.1) and (C.5) exhibits similar behaviours to those obtained for a single channel (cases (S.1) and (S.3), respectively). On the other hand, we notice that the obstacles produce increment in the velocities for the three explicit spacer configurations. This effect is due to the fluid being forced to flow through a reduced cross-section of the channel. For instance, in an empty feed channel with inlet mean feed velocity of $0.1\,m/s$, the maximum velocity achieved is $0.15\,m/s$. In contrast, the maximum velocity using submerged spacers (case (C.2)), is $0.275\,m/s$, whereas for both zig-zag (case (C.3)) and cavity (case (C.4)) spacers, the velocity is $0.265\,m/s$. In turn, in an empty permeate channel with inlet mean permeate velocity of $0.01\,m/s$, the maximum velocity is $0.015\,m/s$, whereas the maximum velocities for the three configurations with explicit spacers are around $0.0289\,m/s$. In addition, when we compare the effect of the obstacles in the feed channel with those of the permeate channel, we observe that the high feed velocities (red regions in Figure 3.6) do not significantly decay along the channel for the zig-zag and cavity spacers. However, in the case (C.2) there is an increment of the velocity near the membrane and the wall, but this occurs close to the spacers, decreasing the velocity away from them. Also, as shown in Figure 3.7, the submerged obstacles produce the highest pressure drop compared to the other configurations. In addition, we observe similar pressure drops when we use the zig-zag or cavity configurations. Now, an unavoidable effect due to the use of spacer-filled channels, is the formation of recirculation zones. This is a particular issue for spacers placed on the surface of the membrane, where it is desirable to have a concentration to be as low as possible [28]. For submerged spacers (C.2), the recirculation is located in the centre of the channel behind the spacers (Figure 3.6, second panel), and away from

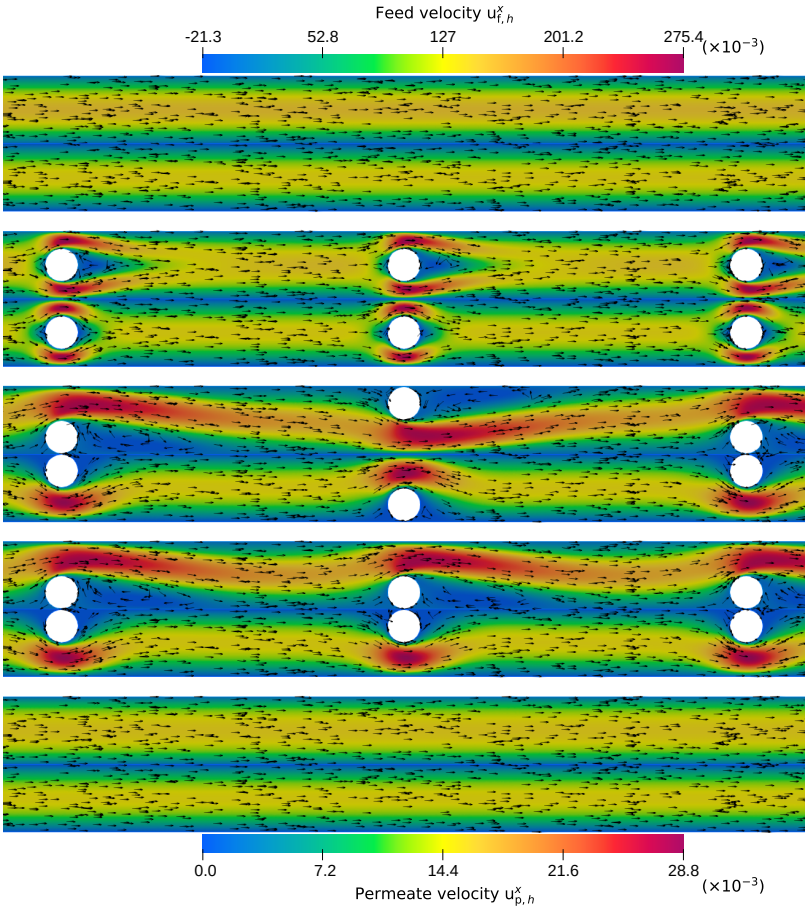

Figure 3.6: Axial velocities in the region $[3, 12]\,mm \times [0, 1.48]\,mm$. From top to bottom: cases (C.1), (C.2), (C.3), (C.4) and (C.5). Simulation conditions: $u_{in,f} = 0.1\,m/s$, $u_{in,p} = 0.01\,m/s$, $\Delta P = \Delta P_2$.

the membrane. In contrast, the recirculation effect for the other two cases not only covers a larger region, but also occurs close to the membrane, as it is immediately evident from Figure 3.6 (third and fourth panels). Here, cavity spacer configuration produces a larger recirculation zones compared to the zig-zag spacers configuration. This leads to strong concentration in the regions close to the spacers that attached to the membrane, as depicted in the third and fourth panels of Figure 3.8. In turn, the middle spacer in case (C.3) has a positive effect in lowering the values of the concentration near the membrane. It is evident that the fluid permeating through the membrane has a lower concentration than the inlet permeate concentration as we observe in the bottom channels of Figure 3.8. This difference since the former is 99% less than the latter. In Figure 3.9 we show the behaviour of the concentration in the feed channel immediately to the left and to the right of the middle spacer along the vertical lines at $x = 7.3\,mm$ and $x = 7.7\,mm$, $y \in [0.74, 1.15]\,mm$, for the five cases. We observe that (C.4) is the case that shows the highest concentration near the membrane. Moreover, an abrupt increment is observable when we compare the region at the left (left panel) of the spacer with the one of the right (right panel).

In Figure 3.10, we display the values of the variables of interest at the membrane from the side of the feed channel. The concentration/permeate velocity in cases (C.3) and (C.4) shows the highest/lowest local maxima/minima of all proposed configurations in the places where the spacers are attached to the membrane. This validates the fact that the concentration has a direct effect on the permeate velocity (third equation of the first row in (2.27)). On the other hand, we observe in the top-left panel, that case (C.2) has the highest pressure drop, whereas case (C.3) has a similar behaviour in pressure drop to that of case (C.4). This behaviour is also similar for the pressure at the membrane (left panel) in the permeate channel, as shown in Figure 3.11, where we plot the pressure and concentration at the membrane from the permeate channel. However, the concentration on the membrane in the permeate channel (right panel) has a larger reduction for configurations (C.3) and (C.4). This is caused by the effect of the spacers attached to the membrane.

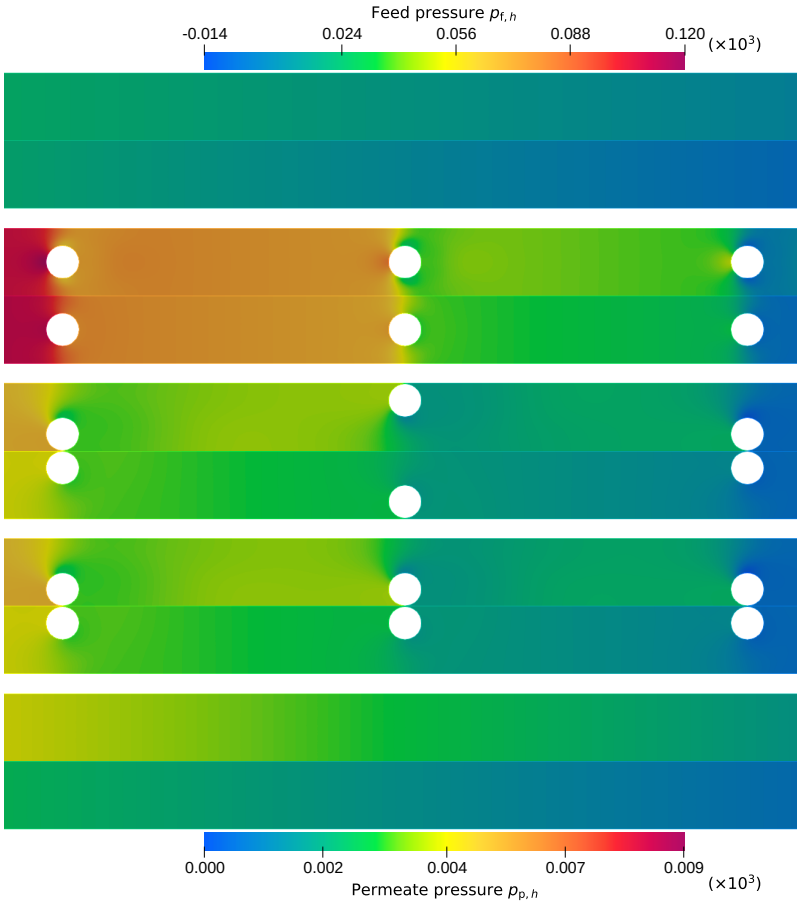

Figure 3.7: Pressure drop in the region $[3, 12]\,mm \times [0, 1.48]\,mm$. From top to bottom: cases (C.1), (C.2), (C.3), (C.4) and (C.5). Simulation conditions: $\mathrm{u}_{\mathrm{in,f}} = 0.1\,m/s$, $\mathrm{u}_{\mathrm{in,p}} = 0.01\,m/s$, $\Delta P = \Delta P_2$.

We now compute the total permeate flow per unit length $\dot{V}/W$ (cf. (3.4)) for the coupled channels configurations. In contrast to the single channel configurations, in this case the total permeate flow per unit length depends on both, the feed and permeate concentrations on the membrane, according to the third equation of the first row in (2.27). We show in Table 3.5 the permeate production for the all coupled configurations. In the particular cases when we use explicit spacers, we observe that the largest permeate production is due to the submerged spacers configuration, while the cavity spacer configuration is the lowest. To see this more clearly, in Table 3.6, we show the increment ($\rightarrow$) rates of the values of the total permeate flow per unit length $\dot{V}/W$ reported in Table 3.5, where having submerged spacers produces 1.87% of increment in $\dot{V}/W$ compared to the empty channel configuration. In this table, we also want to compare how well implicit spacers emulates the different cases of explicit spacers. We observe that case (C.5) always has a larger permeate flux than case (C.1). This implies that the use of implicit spacers tends to emulate those cases where explicit spacers also reduce the salt concentration compared to case (C.1). From the latter, we note that the porous case emulates more accurately the case (C.2), since differs by only 0.86%.

	(C.1)	(C.2)	(C.3)	(C.4)	(C.5)
$\dot{V}/W\ (m^2/s)$	8.37876×10^{-8}	8.53812×10^{-8}	8.36789×10^{-8}	8.27399×10^{-8}	8.46516×10^{-8}

Table 3.5: Total permeate flow per unit length $\dot{V}/W$ in coupled channels for $\mathrm{u}_{\mathrm{in,f}} = 0.1\,m/s$, $\mathrm{u}_{\mathrm{in,p}} = 0.01\,m/s$ and $\Delta P = \Delta P_2$, of the five cases (C.1), (C.2), (C.3), (C.4) and (C.5).

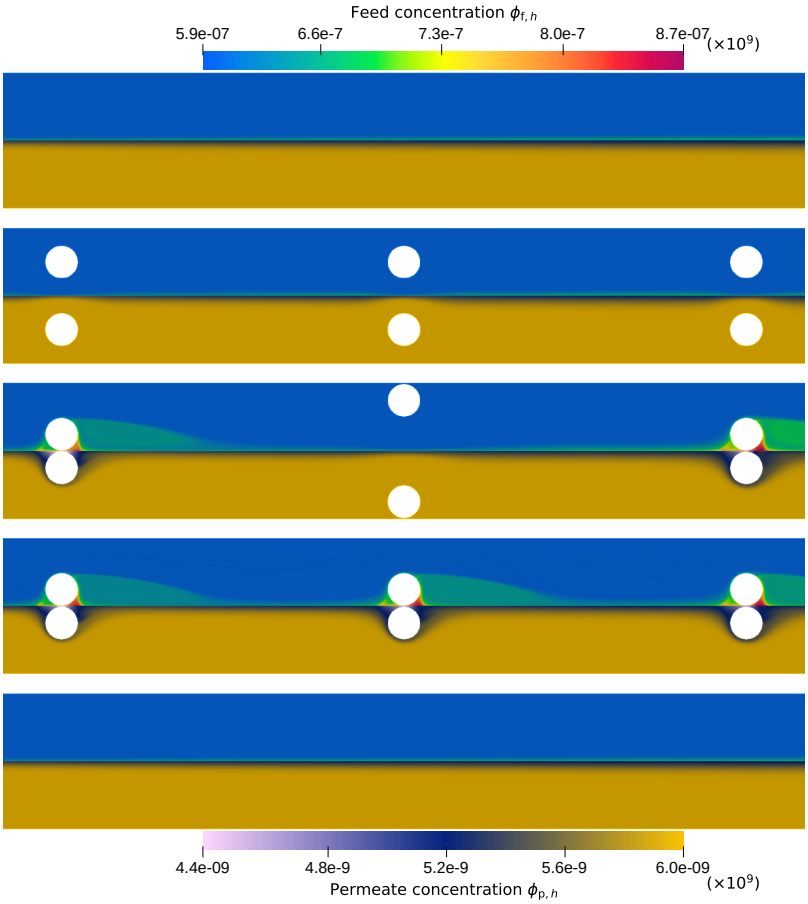

Figure 3.8: Salt concentration in the region $[3, 12]\,mm \times [0, 1.48]\,mm$. From top to bottom: cases (C.1), (C.2), (C.3), (C.4) and (C.5). Simulation conditions: $\mathrm{u}_{\mathrm{in,f}} = 0.1\,m/s$, $\mathrm{u}_{\mathrm{in,p}} = 0.01\,m/s$, $\Delta P = \Delta P_2$.

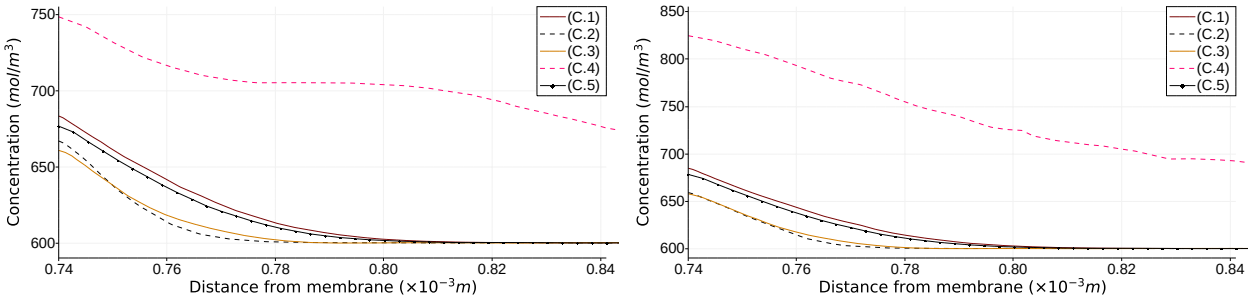

Figure 3.9: Salt concentration along the vertical lines at $x = 7.3\,mm$ (left panel) and $x = 7.7\,mm$ (right panel), $y \in [0.74, 1.15]\,mm$ for the five cases (C.1), (C.2), (C.3), (C.4) and (C.5). Simulation conditions: $\mathrm{u}_{\mathrm{in,f}} = 0.1\,m/s$, $\mathrm{u}_{\mathrm{in,p}} = 0.01\,m/s$, $\Delta P = \Delta P_2$.

(C.1) $\xrightarrow{1.87\%}$ (C.2)	(C.4) $\xrightarrow{1.27\%}$ (C.1)	(C.5) $\xrightarrow{0.86\%}$ (C.2)	(C.4) $\xrightarrow{2.26\%}$ (C.5)
(C.3) $\xrightarrow{0.13\%}$ (C.1)	(C.1) $\xrightarrow{1.02\%}$ (C.5)	(C.3) $\xrightarrow{1.14\%}$ (C.5)	

Table 3.6: Increment rate in the value of $\dot{V}/W$ reported in Table 3.5, with respect to the variation of configurations.

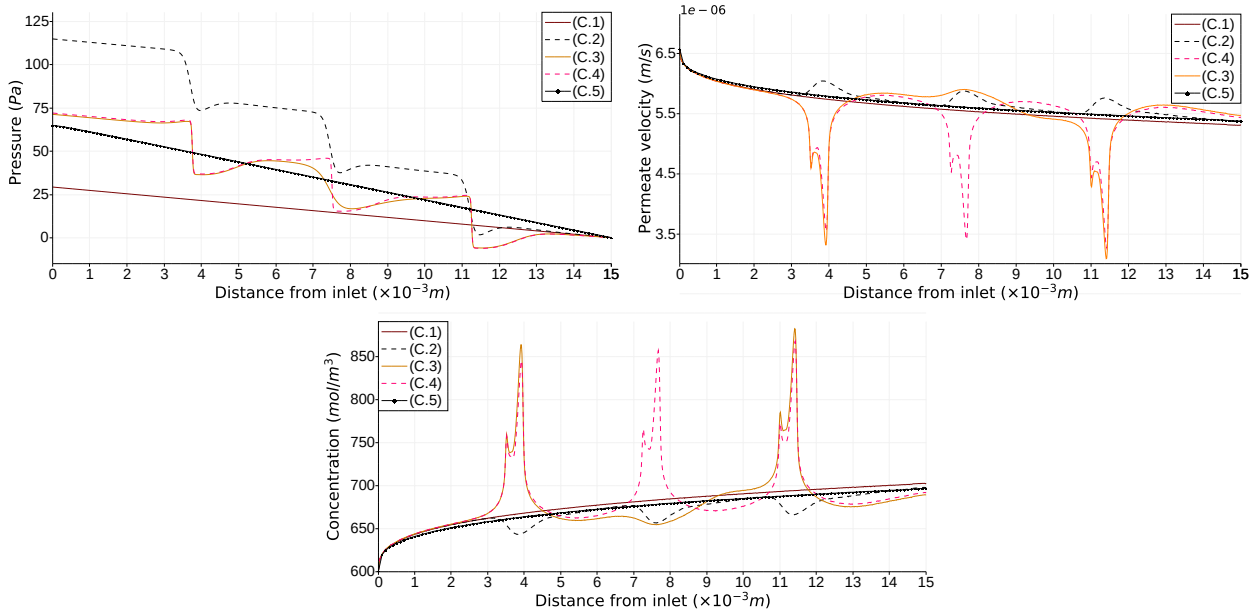

Figure 3.10: Feed channel. Relative pressure drop (top-left panel), permeate velocity (top-right panel) and concentration level (bottom panel) at the membrane ($y = 0.74\,mm$) for all cases (C.1)-(C.5). Simulation conditions: $\mathrm{u_{in,f}} = 0.1\,m/s$, $\mathrm{u_{in,p}} = 0.01\,m/s$, $\Delta P = \Delta P_2$.

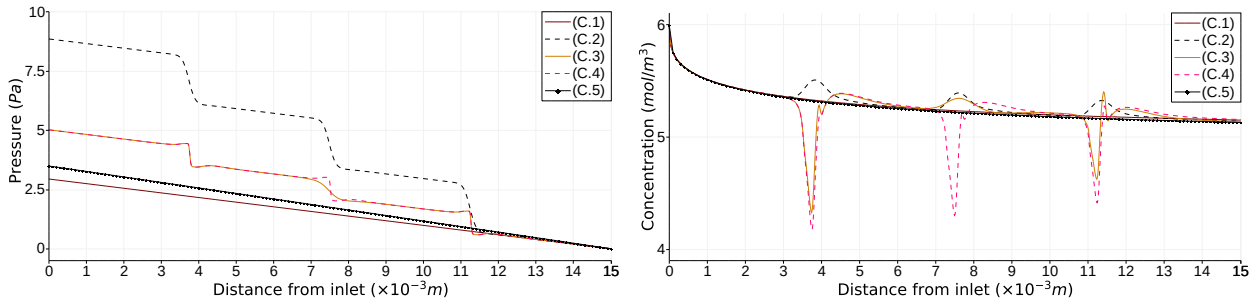

Figure 3.11: Permeate channel. Relative pressure drop (left panel) and concentration level (right panel) at the membrane ($y = 0.74\,mm$) for all cases (C.1)-(C.5). Simulation conditions: $\mathrm{u_{in,f}} = 0.1\,m/s$, $\mathrm{u_{in,p}} = 0.01\,m/s$, $\Delta P = \Delta P_2$.

4 Conclusions

A new numerical model based on two-dimensional mixed finite element method has been used to study the fluid flow patterns, concentration of salt, pressure losses and permeate flow in desalination channels in the context of RO. The simulations are performed in a Reynolds number range for laminar flow less than 170, typical of sea water membrane module operation. They are based on two different perspectives, the first using the Navier–Stokes coupled to transport equations for the case of empty channels, and also for different configurations of explicit spacers. The second perspective circumvents the high computational cost of including the spacers and instead handles them as a homogeneous porous medium in the entire domain by means of the Brinkman–Forchheimer equation, also coupled to transport equation. The former perspective, shows similar results in terms of relevant values such as permeate flux, pressure behaviour and velocity, compared to previous works. The latter alternative has shown significant potential to provide comparative results to those cases where explicit spacers also reduce the salt concentration compared to case of empty channels. In our simulations, the case with explicit submerged spacers is emulated more closely, showing that the deviation is only 0.86%. To the best of our knowledge, this is the first work that considers the two channel coupled configurations, and our simulations can be used as a benchmark. Furthermore, our work suggests that under same parameters, different positions of the spacers in the channel configuration lead to different fluid patterns, which in turn generate a

local increment or reduction in the concentration of salt. Also, a higher local concentration on the membrane, leads in a lower permeate velocity. On the other hand, the models studied in this paper, constitutes a stepping stone to simulate fouling at membranes. Further work is needed for the evaluation of fouling, where transient state is necessary to account for. This is part of an ongoing research.

References

[1] A. Ahmad, K. Lau, and M. Abu Bakar, *Impact of different spacer filament geometries on concentration polarization control in narrow membrane channel*, Journal of Membrane Science, 262 (2005), pp. 138–152.

[2] F. E. Ahmed, A. Khalil, and N. Hilal, *Emerging desalination technologies: Current status, challenges and future trends*, Desalination, 517 (2021), p. 115183.

[3] I. Babuška and G. N. Gatica, *On the mixed finite element method with Lagrange multipliers*, Numer. Methods Partial Differential Equations, 19 (2003), pp. 192–210.

[4] A. S. Berman, *Laminar Flow in Channels with Porous Walls*, Journal of Applied Physics, 24 (1953), pp. 1232–1235.

[5] P. V. Bulat and K. N. Volkov, *Simulation of incompressible flows in channels containing fluid and porous regions*, International Journal of Industrial and Systems Engineering, 34 (2020), pp. 283–300.

[6] J. Camaño, C. García, and R. Oyarzúa, *Analysis of a momentum conservative mixed-FEM for the stationary Navier-Stokes problem*, Numer. Methods Partial Differential Equations, 37 (2021), pp. 2895–2923.

[7] J. Camaño and R. Oyarzúa, *A conforming and mass conservative pseudostress-based mixed finite element method for Stokes*, Preprint 2023-15, Centro de Investigación en Ingeniería Matemática (CI^2MA), Universidad de Concepción, (2023).

[8] N. Carro, D. Mora, and J. Vellojin, *A finite element model for concentration polarization and osmotic effects in a membrane channel*, International Journal for Numerical Methods in Fluids, 96 (2024), pp. 601–625.

[9] S. Caucao, R. Oyarzúa, and S. Villa-Fuentes, *A new mixed-FEM for steady-state natural convection models allowing conservation of momentum and thermal energy*, Calcolo, 57 (2020).

[10] T. A. Davis, *Algorithm 832: UMFPACK V4.3—an unsymmetric-pattern multifrontal method*, ACM Trans. Math. Software, 30 (2004), pp. 196–199.

[11] J. Eke, A. Yusuf, A. Giwa, and A. Sodiq, *The global status of desalination: An assessment of current desalination technologies, plants and capacity*, Desalination, 495 (2020), p. 114633.

[12] G. N. Gatica, *A Simple Introduction to the Mixed Finite Element Method. Theory and Applications*, SpringerBriefs in Mathematics. Springer, Cham, 2014.

[13] G. N. Gatica, R. Oyarzúa, and F.-J. Sayas, *Analysis of fully-mixed finite element methods for the Stokes-Darcy coupled problem*, Math. Comp., 80 (2011), pp. 1911–1948.

[14] P. H. Gleick, *Water in crisis*, Pacific Institute for Studies in Dev., Environment & Security. Stockholm Env. Institute, Oxford Univ. Press. 473p, 9 (1993), pp. 1051–0761.

[15] F. Hecht, *New development in freefem++*, J. Numer. Math., 20 (2012), pp. 251–265.

[16] L. Huang and M. T. Morrissey, *Finite element analysis as a tool for crossflow membrane filter simulation*, Journal of Membrane Science, 155 (1999), pp. 19–30.

[17] J. Johnston, S. M. Dischinger, M. Nassr, J. Y. Lee, P. Bigdelou, B. D. Freeman, K. L. Gleason, D. Martinand, D. J. Miller, S. Molins, N. Spycher, W. T. Stringfellow, and N. Tilton, *A reduced-order model of concentration polarization in reverse osmosis systems with feed spacers*, Journal of Membrane Science, 675 (2023), p. 121508.

[18] J. Johnston, J. Lou, and N. Tilton, *Application of projection methods to simulating mass transport in reverse osmosis systems*, Computers & Fluids, 232 (2022), p. 105189.

[19] C. Kleffner, G. Braun, and S. Antonyuk, *Influence of membrane intrusion on permeate-sided pressure drop during high-pressure reverse osmosis*, Chemie Ingenieur Technik, 91 (2019), pp. 443–454.

[20] A. Lenci, F. Zeighami, and V. Di Federico, *Effective forchheimer coefficient for layered porous media*, Transport in Porous Media, 144 (2022), pp. 459–480.

[21] J. Liu, *Open and traction boundary conditions for the incompressible navier–stokes equations*, Journal of Computational Physics, 228 (2009), pp. 7250–7267.

[22] S. Ma, L. Song, S. L. Ong, and W. J. Ng, *A 2-d streamline upwind Petrov/Galerkin finite element model for concentration polarization in spiral wound reverse osmosis modules*, Journal of Membrane Science, 244 (2004), pp. 129–139.

[23] V. Perfilov, A. Ali, and V. Fila, *A general predictive model for direct contact membrane distillation*, Desalination, 445 (2018), pp. 181–196.

[24] V. Perfilov, V. Fila, and J. Sanchez Marcano, *A general predictive model for sweeping gas membrane distillation*, Desalination, 443 (2018), pp. 285–306.

[25] R. Schulz, N. Ray, S. Zech, A. Rupp, and P. Knabner, *Beyond Kozeny–Carman: Predicting the permeability in porous media*, Transport in Porous Media, 130 (2019), pp. 487 – 512.

[26] J. Schwinge, D. E. Wiley, and D. F. Fletcher, *Simulation of the flow around spacer filaments between channel walls. 2. mass-transfer enhancement*, Industrial & Engineering Chemistry Research, 41 (2002), pp. 4879–4888.

[27] C. Skuse, A. Gallego-Schmid, A. Azapagic, and P. Gorgojo, *Can emerging membrane-based desalination technologies replace reverse osmosis?*, Desalination, 500 (2021), p. 114844.

[28] A. Subramani, S. Kim, and E. M. Hoek, *Pressure, flow, and concentration profiles in open and spacer-filled membrane channels*, Journal of Membrane Science, 277 (2006), pp. 7–17.

[29] L. Xu, S. Xu, X. Wu, P. Wang, D. Jin, J. Hu, L. Li, L. Chen, Q. Leng, and D. Wu, *Heat and mass transfer evaluation of air-gap diffusion distillation by ε-ntu method*, Desalination, 478 (2020), p. 114281.

Centro de Investigación en Ingeniería Matemática (CI^{2}MA)

PRE-PUBLICACIONES 2024

2024-04 Rommel Bustinza, Matteo Cicuttin, Ariel Lombardi: *A Hybrid High-Order method for the mixed Steklov eigenvalue problem*

2024-05 Isaac Bermudez, Jaime Manríquez, Manuel Solano: *A hybridizable discontinuous Galerkin method for Stokes/Darcy coupling in dissimilar meshes*

2024-06 Thomas Führer, Diego Paredes: *Robust hybrid finite element methods for reaction-dominated diffusion problems*

2024-07 Raimund Bürger, Enrique D. Fernández Nieto, Jorge Moya: *A multilayer shallow water model for tsunamis and coastal forest interaction*

2024-08 Fernando Betancourt, Raimund Bürger, Stefan Diehl, María Carmen Martí, Yolanda Vásquez: *A degenerating convection-diffusion model of a flotation column: theory, numerics and applications*

2024-09 Fernando Betancourt, Raimund Bürger, Julio Careaga, Lucas Romero: *Coupled finite volume methods for settling in inclined vessels with natural convection*

2024-10 Kaïs Ammari, Vilmos Komornik, Mauricio Sepúlveda, Octavio Vera: *Stability of the Rao-Nakra sandwich beam with a dissipation of fractional derivative type: theoretical and numerical study*

2024-11 Lady Angelo, Jessika Camaño, Sergio Caucao: *A skew-symmetric-based mixed FEM for stationary MHD ows in highly porous media*

2024-12 Gabriel N. Gatica: *A note on the generalized Babuska-Brezzi theory: revisiting the proof of the associated Strang error estimates*

2024-13 Carlos D. Acosta, Raimund Bürger, Julio Careaga, Stefan Diehl, Romel Pineda, Daniel Támara: *A semi-implicit method for a degenerating convection-diffusion-reaction problem modeling secondary settling tanks*

2024-14 Gabriel N. Gatica, Cristian Inzunza, Ricardo Ruiz-Baier: *Primal-mixed finite element methods for the coupled Biot and Poisson-Nernst-Planck equations*

2024-15 Isaac Bermudez, Víctor Burgos, Jessika Camaño, Fernando Gajardo, Ricardo Oyarzúa, Manuel Solano: *Mixed finite element methods for coupled fluid flow problems arising from reverse osmosis modeling*

Para obtener copias de las Pre-Publicaciones, escribir o llamar a: Director, Centro de Investigación en Ingeniería Matemática, Universidad de Concepción, Casilla 160-C, Concepción, Chile, Tel.: 41-2661324, o bien, visitar la página web del centro: `http://www.ci2ma.udec.cl`




Centro de Investigación en
Ingeniería Matemática (CI²MA)
Universidad de Concepción

Casilla 160-C, Concepción, Chile
Tel.: 56-41-2661324/2661554/2661316
http://www.ci2ma.udec.cl